A THEORETICAL STUDY ON DRY REFORMING OF METHANE (CDRM) OVER COBALT METAL

by

Vasfiye Çimenoğlu

B.S., Chemical Engineering, Boğaziçi University, 2009

Submitted to the Institute for Graduate Studies in
Science and Engineering in partial fulfillment of
the requirements for the degree of
Master of Science

Graduate Program in Chemical Engineering
Boğaziçi University

2011

to my family

ACKNOWLEDGEMENTS

First of all, I would like to express my truthful gratitude to my thesis supervisor Prof. Ahmet Erhan Aksoylu, who devoted his valuable time to guiding me, helping me and motivating me all the time. It was a great honor for me to work with him during my undergraduate and graduate thesis, where I learned from his great expertise and experiences in catalysis and reaction engineering.

I am very grateful to my thesis committee members, Assoc. Prof. Hasan Bedir and Prof. Ramazan Yıldırım, sparing their valuable time for reading and commenting on my thesis.

I offer many thanks to a special colleague, Ali Uzun, my lab mate in KB 411-A, for his friendship and giving me endless support, valuable advice and motivation during my study.

I also would like to express my great appreciation for Aslıhan Sümer for his great contribution during by teaching me Material Studio.

Burcu Selen Çağlayan, Feyza Gökaliler and Tuğba Davran Candan deserve special thanks as my mentors. Their invaluable experience and will to help has made this study possible.

Heartfelt thanks goes to my friends, Melek Selcen Başar, Aysun İpek Paksoy, Merve Eropak, Mine Nilay Aktemur, İrfan Hösükoğlu and Aybüke Leba.

Special thanks to Murat Örok for helping me during my study with his patience and care.

Finally, I would like to express my dearest thanks to all my family members for their patience, encouragement and moral support throughout my whole education. Their endless

love and trust in me was what made me motivated all the time. This is why I dedicate this work to them.

The graduate scholarship provided by TÜBİTAK for my M.S. studies deserves thankful recognition. Financial support provided by State Planning Organization of Turkey through project DPT 07K120630 and by Boğaziçi University Research Fund through project BAP 5570 are gratefully acknowledged.

ABSTRACT

A THEORETICAL STUDY ON DRY REFORMING OF METHANE (CDRM) OVER COBALT METAL

The aim of this study is to analyze the adsorption and reaction steps of CDRM on the Co(111) surface by using DFT calculations. In this context, the adsorption/coadsorption of reactants, reaction intermediates, and the reaction were studied. LDOS analysis was also used whenever detailed analysis is necessary. In this study, adsorption behaviours of all reactants some products and intermediate products of CDRM reaction were investigated first. CO_2 was adsorbed on all sites of Co(111) surface but adsorption energies and LDOS profiles show that the strengths of CO_2 adsorption on those sites are very low. On the other hand, CH_4 adsorption is either unstable or yields CH_3 and H stabilized on the surface. CO adsorptions on all sites were found very strong with very similar adsorption energies. CH_3 adsorption is stable on all sites, except on the bridge site, and the adsorption is strong. CH_3 initially placed at bridge position assumed H_{hcp} position upon energy optimization. The most favorable sites for CH_3 and CO adsorptions were H_{hcp} and atop sites, respectively. Simulation results show that oxygen adsorption is stable only at H_{hcp} site as O adsorbed on other sites assume H_{hcp} position upon energy optimization. In the second part of the work, 'C and O', and 'CO and CH_3' coadsorption systems were studied for different surface concentration and adsorption configuration combinations. C and O coadsorption studies revealed that the energy optimized structures are very sensitive to relative surface coverages of the adsorbates as well as whether there is site competition between them; C and O interaction yield CO only when there is site competition. Finally, the TS searches of CH_4 dehydrogenation and CO formation were carried out to obtain the reaction pathways and activation energies of elementary steps. CH_4 dehydrogenation step was found as the rate-determining step of hydrogen and surface carbon production. Since CH dehydrogenation has high energy barrier and the strong endothermicity, CH dehydrogenation was found unfavorable both kinetically and thermodynamically. On the other hand, CO formation is an exothermic process and was found favorable.

ÖZET

KOBALT METALİNDE METANIN KURU REFORMLANMASI ÜZERİNE TEORİK ÇALIŞMA

Bu tezin amacı, DFT hesaplamaları kullanılarak Co(111) yüzeyi üzerinde methanın karbon dioksitle reformlaması reaksiyonun (CDRM) adımlarını ve onun adsorpsiyonunu analiz etmektir. Bu bağlamda, adsorpsiyon/koadsorpsiyon reaktantları, reaksiyon ara ürünleri ve reaksiyon çalışıldı. LDOS analizi, gerektiğinde kullanıldı. Öncelikle CDRM'nin tüm reaktantlarının, bazı ürün ve yan ürünlerinin adsorpsiyon davranışları araştırıldı. CO_2 Co(111) yüzeyinin tüm sitelerine adsorp edildi, fakat adsorpsiyon enerjileri ve LDOS profilleri CO_2 adsorpsiyonunun güçlerinin çok düşük olduğunu gösterdi. Bunun yanında, CH_4 adsorpsiyonu dengesizdir veya yüzey üzerinde dengeli olan CH_3 ve H verir. CO adsorpsiyonları benzer adsorpsiyon enerjileri ile bütün siteler üzerinde güçlü bulundu. CH_3 adsorpsiyonu, köprü sitesi hariç bütün siteleri üzerinde dengelidir. İlk önce köprü pozisyonuna konulan CH_3, enerji optimizasyonu sonucu altıgensel sıkı istifli (hcp) pozisyona gitti. CH_3 ve CO adsorpsiyonları için en uygun siteler sırasıyla, hcp ve tepe pozisyonlarıdır. Simulasyon sonuçları, O'nun sadece hcp sitesinde dengede olduğunu; öyle ki diğer sitelere adsorplanan O enerji optimizasyonu sonucu hcp pozisyona gittiğini gösterir. Çalışmanın ikinci kısmında, 'C ve O' ve 'CO ve CH_3' koadsorpsiyon sistemleri farklı yüzey konsantrasyonları ve adsorpsiyon konfigurasyonları için çalışıldı. C ve O koadsorpsiyon çalışmaları, ilk coadsorpsiyon sistemleri arasında site rekabeti varsa enerji açısından optimize olmuş yapıların adsorbantların relatif yüzey kaplamasına çok duyarlı olduğunu; ilk coadsorpsiyon sistemleri için site rekabeti olduğunda C ve O etkileşiminin CO verdiğini ortaya çıkardı. Sonuç olarak, reaksiyon yolu ve ara basamakların aktivasyon enerjilerine ulaşmak için CH_4 dehidrasyou ve CO oluşumunun TS çalışmaları yapıldı. Metanın hidrojen giderme aşaması, metanın ayrılmalı adsorpsiyonun oran belirleme ve yüzey karbonu üretme aşaması olarak olarak bulundu. CH'ın hidrojen gidermesi yüksek enerji bariyerine ve güçlü endotermikliğe sahip olduğu için, kinetik ve termodinamik açıdan elverişli değildir. Buna karşın CO oluşması ekzotermiktir, bu nedenle elverişlidir.

TABLE OF CONTENTS

ACKNOWLEDGEMENT iv
ABSTRACT vi
ÖZET vii
LIST OF FIGURES x
LIST OF TABLES xiii
LIST OF SYMBOLS..... xiv
ACRONYMS/ABBREVIATIONS..... xv
1. INTRODUCTION …..... 1
2. LITERATURE SURVEY 4
2.1. Carbon Dioxide Reforming of Methane 4
2.2. Reaction Mechanism of CDRM..... 6
2.3. Catalysts for CDRM ……..……..…….…. 9
2.3.1. Co-based Catalysts ……..…… 12
2.3.1.1. Experimental Studies 12
2.3.1.2. Computational Studies …….…….... 15
2.3.2. Deactivation of Catalysts ……... 17
3. METHODOLOGY..... 22
3.1. Theory behind Computational Methods: Quantum Chemical Models 22
3.1.1. Schrödinger Equation …..... 23
3.1.2. Many-body Problem..... 23
3.1.3. Electron-electron Interactions ……..... 24
3.1.3.1. Density Functional Models ……. 24
3.1.4. Periodic Supercells ……. 26
3.1.5. Bloch's Theorem ……. 27
3.1.6. K-point Sampling ……... 27
3.1.7. Plane-Wave Basis Set ……. 28
3.1.8. Plane-Wave Representation of Kohn-Sham Equations ……..... 28
3.1.9. Electron-Ion Interactions (Pseudopotential Theory) …….. 29
3.2. Material Studio Software 29

3.2.1. MS Visualizer……..... 29
3.2.2. MS CASTEP ……..... 31
3.2.3. MS DMol3 …….. 31
3.3. Parameters for Optimization ……..... 32
3.4. Calculating the Properties …..... 33
3.4.1. LDOS Charts 33
3.4.2. Mulliken Charges ……..... 34
4. RESULTS AND DISCUSSION 35
4.1. Calculational Parameters……..…….…… 35
4.2. CO_2 Adsorption on Co(111) ……..…….…… 37
4.3. CH_4 Adsorption on Co(111)..... 40
4.4. CH_3 Adsorption on Co(111) …..... 42
4.5. CO Adsorption on Co(111) ……. 44
4.6. O Adsorption on Co(111) ……... 47
4.7. Methane Dehydrogenation …….. 49
4.8. Effect of Surface Coverage on Coadsorption of C+O…….……..... 52
4.9. CO and CH_3 Coadsorption ……..... 58
4.10. CO Formation from C+O ……..... 62
5. CONCLUSIONS AND RECOMMENDATIONS 64
5.1. Conclusions 64
5.2. Recommendations 65
REFERENCES 66

LIST OF FIGURES

Figure 3.1.	The Co unit cell. Dark balls represent Co atoms.……	30
Figure 3.2.	The side view of p(2x2) surface unit cell of Co(111)……..	30
Figure 3.3.	A sample energy curve obtained fater LST algorithm...……..…….	32
Figure 4.1.	Ball model of Co(111) and various CO_2 adsorption sites available on the surface. Sites are labeled as T (atop), B (bridge), H_{hcp} (hollow hcp) and H_{fcc} (hollow fcc)…..……..	37
Figure 4.2.	Changes in LDOS (a) C of adsorbed CO_2 molecule on H_{hcp} site (b) C of adsorbed CO_2 molecule on H_{fcc} site (c) atop CO_2-coordinated Co atom at 0.25 ML.……...…….	39
Figure 4.3.	CO_2 adsorption on H_{hcp} site at 0.25 ML.…….	40
Figure 4.4.	Changes in LDOS atop CH_4-coordinated Co atom at 0.25 ML.…….	42
Figure 4.5.	Changes in LDOS C of adsorbed CH_3 molecule on H_{hcp} at 0.25 ML.	44
Figure 4.6.	Changes in LDOS (a) atop CO-coordinated Co atom (b) H_{hcp} CO-coordinated Co atom (c) C of adsorbed CO molecule at 0.25 ML.….	46
Figure 4.7.	Initial and final structures of O adsorption on bridge site at 0.25 ML	48
Figure 4.8.	Changes in LDOS (a) H_{hcp} O-coordinated Co atom (b) O molecule at 0.25 ML..…….....	49

Figure 4.9. TS searches of CH_4 sequential dehydrogenation and the energy barriers (Ha)……...……. 51

Figure 4.10. (a) The top view of initial structure of the coadsorption of O at H_{fcc} site and C at H_{hcp} site (b) The change of the initial structure of coadsorption of O and C to the final structure..... 53

Figure 4.11. (a) The top view of initial structure of the coadsorption of O at atop site and C at atop site (b) The change of the initial structure of coadsorption of O and C to the final structure..... 54

Figure 4.12. (a) The top view of initial structure of the coadsorption of 2O at atop and H_{hcp} sites and C at atop site (b) The change of the initial structure of coadsorption of 2O and C to the final structure..... 55

Figure 4.13. (a) The top view of initial structure of the coadsorption of 2O at atop sites and C at atop site (b) The change of the initial structure of coadsorption of 2O and C to the final structure..... 56

Figure 4.14. (a) The top view of initial structure of the coadsorption of O at H_{hcp} site and 2C at atop sites (b) The change of the initial structure of coadsorption of O and 2C to the final structure..... 57

Figure 4.15. (a) The top view of initial structure of the coadsorption of O at atop site and 2C at atop sites (b) The change of the initial structure of coadsorption of O and 2C to the final structure..... 58

Figure 4.16. (a) The top view of initial structure of the coadsorption of CO at H_{hcp} site and CH_3 at H_{hcp} site (b) The change of the initial structure of coadsorption of CO and CH_3 to the final structure..... 59

Figure 4.17. (a) The top view of initial structure of the coadsorption of CO at H_{fcc}-H_{hcp} sites and CH_3 at bridge site (b) The change of the initial structure of coadsorption of CO and CH_3 to the final structure…..... 60

Figure 4.18. TS search and the energy barriers (Ha) of CO formation as C+O↔CO…..... 62

LIST OF TABLES

Table 4.1. Energy of CO_2 adsorption on Co(111). The values correspond to total adsorption energy per unit cell. The distance of C from the nearest Co atom is exhibited as d(Co-C).……...……. 38

Table 4.2. Energy of CH_4 adsorption on Co(111). The values correspond to total adsorption energy per unit cell. The distance of C from the nearest Co atom is exhibited as d(Co-C).....…… 41

Table 4.3. Energy of CH_3 adsorption on Co(111). The values correspond to total adsorption energy per unit cell. The distance of C from the nearest Co atom is exhibited as d(Co-C).…… 42

Table 4.4. Energy of CO adsorption on Co(111). The values correspond to total adsorption energy per unit cell. The distance of C from the nearest Co atom is exhibited as d(Co-C)……..... 44

Table 4.5. Energy of O adsorption on Co(111). The values correspond to total adsorption energy per unit cell. The distance of O from the nearest Co atom is exhibited as d(Co-O).…… 48

Table 4.6. Energetics of the most favored elementary steps in CH_4 dehydrogenation on Co(111).…….. 50

Table 4.7. Adsorption types and system total energies C+O coadsorptions on Co(111)..... 52

Table 4.8. Adsorption types, system total and total coadsorption energies of C+O coadsorptions on Co(111).……..... 61

LIST OF SYMBOLS

B	Bridge
C	Coefficient
D	Distance
E	Energy
E_{ads}	Adsorption energy
E_{coads}	Coadsorption energy
E_j	Hatree Coulomb term of energy
E_T	Electron energy
E_{xc}	Exchange-correlation energy
E_V	Electron-nuclear interaction energy
F	Exchange/correlation functional
G	Reciprocal lattice vector
H	Hollow
K	Wave vector
P	Density matrix
R	Distance between the nucleus and the electron
S	Overlap matrix
T	Atop
V_H	Hatree potential
V_{ion}	Ion potential
V_{XC}	Exchange/correlation potential
Z	Nuclear charge
ε_{xc}	Exchange-correlation energy per electron
$\hat{H}$	Hamiltonian operator
$\mu\nu\|\lambda\sigma$	Two-electron integrals
P	Total electron density
Φ	Molecular orbital coefficient
Ψ	Kohn-Sham orbitals

LIST OF ACRONYMS/ABBREVIATIONS

AE	All Electron
CATREL	Catalysis and Reaction Engineering Laboratory
CDRM	Carbon Dioxide Reforming of Methane
CETS	Chemical Energy Transmission Systems
CI	Configuration Interaction Model
CoAlCO-IM	Cobalt-based Catalysts Prepared by Conventional Impregnation on γ-Al_2O_3 Support
CoAlSG	Cobalt-based Catalysts Prepared by Direct Sol-gel Processing on γ-Al_2O_3 Support
CoAlSG-IM	Cobalt-based Catalysts Prepared by Sol-gel-made Catalyst on γ-Al_2O_3 Support
DFT	Density Functional Theory
DNP	Double-numeric Quality Basis Set with Polarization Functions
DRIFTS	Diffuse Reflectance Infrared Fourier Transform Spectroscopy
NEXAFS	Near-edge X-ray Absorption Fine Structure Spectroscopy
GGA	Generalized-gradient Approximation
IR	Infrared
LST	Linear Synchronous Transit Maximation
LDA	Local-density Approximation
LDOS	Local Density of States
MP	Møller-Plesset Model
MP2	Second Order Møller-Plesset Model
MS	Material Studio
PBE	Perdew-Burke-Ernzerhof Functional
QST	Quadratic Synchronous Transit Maximization
SCF	Self-consistent Field
TG-DTA	Thermo Gravimetry/Differential Thermal Analyzer

TS	Transition State
XRD	X-ray Diffraction
XPS	X-ray Photoelectron Spectroscopy
VASP	The Vienna Ab-initio Simulation Package

1. INTRODUCTION

The word's energy demand is growing as a result of the industrial development, so efficient production and use of clean energy have become particularly important and urgent. As concerns with environment protection is increasing, new energy production techniques will be needed aiming to reduce the emission of greenhouse gasses to the atmosphere. Hydrogen is a preferable energy carrier, and can be obtained from fossil fuels such as methane, or renewable resources such as biogas and methanol. Natural gas is an important and widely used hydrogen source in industry (Dadyburjor *et al.,* 2009). The natural gas, which consists mostly methane (80%) and heavier hydrocarbons, CO_2 and a complex mixture of other gases like ethane, propane, etc., is considered as the fuel of the near future considering its worldwide reserves and fastly depleting crude oil resources (Boukha *et al.,* 2007).

Hydrogen can be obtained from methane by utilizing catalytic technologies such as methane steam reforming, methane partial oxidation and methane dry reforming. Methane dry reforming, in other words carbon dioxide reforming of methane (CDRM), was proposed in recent years as an energy efficient way to use methane resources (Zhu *et al.,* 2010). CDRM has an advantage of producing syngas (H_2+CO) with high purity. Additionally, it uses greenhouse gas CO_2 as the feedstock, which is highly advantageous since it prevents carbon dioxide emission by its direct utilization and converting it to valuable products. The syngas obtained with CDRM has a H_2/CO ratio of 1, and this ratio is favorable for usage of syngas as the feedstock for a variety of downstream processes, such as methanol synthesis, Fischer-Tropsch synthesis or ammonia synthesis (Huang *et al.,* 2010). Since the reaction is highly endothermic, the dry reforming process can be also used in different areas, like a system for solar energy transfer to chemical energy, energy storage in the form of CO and H_2 and also in chemical energy transmission systems (CETS) (Gallego *et al*., 2008a). In addition to these advantages, CDRM can be carried out in areas where water is not available. CDRM is attractive; because this reaction can contribute to the use of natural gas fields containing a large amount of CO_2. By applying CDRM, natural gas containing large amount of CO_2 can be utilized directly without any pre-separation (Cheng *et al.,* 2006). Due to these advantages, considerable works have been performed to

obtain catalysts for CDRM to achieve both high activity and good stability (Huang *et al.,* 2010).

There are some drawbacks of CDRM and the most important one is the requirement high temperatures to achieve high conversion levels due to highly endothermic nature of the process. This requirement causes deactivation of catalysts by coke deposition, and sintering of the metallic phase and support. Coke is formed mainly by two reactions; endothermic methane decomposition and exothermic carbon monoxide disproportionation. The other side reactions of CDRM are the reverse water gas shift, CO and CO_2 methanation reactions, coke gasification and steam reforming (Gallego *et al*., 2008b).

Many mechanisms regarding CDRM reaction have been proposed using different techniques and catalysts for many years. All studies have agreed that reaction mechanism of CDRM began with the dissociative adsorption of methane on the metallic sites of the CDRM catalysts. On the other hand, there is a disagreement on CO_2 adsorption part of the reaction mechanism; some studies have proposed that CO_2 dissociated into surface CO and O on Ni, Ru, Rh, Pd, Ir, and Pt catalysts, but some studies have proposed that CO_2 adsorption was nondissociative (Rostrupnielsen *et al.,* 1993; Erdohelyi*et al.,* 1993; Bradford*et al.,* 1999; Sullivana *et al.,* 2010; Jiao *et al.,* 2006).

The most important factors that affect the performance of CDRM process are activity, selectivity and stability specs of its catalyst. Type(s) of the metal(s) used in catalyst preparation, type of the support, addition of promoters and the conditions of catalyst preparation and pretreatment are the major factors that affect the performance of CDRM catalysts. Different kinds of catalysts have been studied in order to reach high activity, selectivity and stability. Widely studied catalysts are Ni, Co, Rh, Pd, Pt, Ir, Fe and Cu based systems. The most used support types are ZrO_2, Al_2O_3, MgO, ZrO_2-La_2O_3, La_2O_3, SiO_2, TiO_2, $ZnOCeO_2$-ZrO_2 and CeO_2 (Bradford *et al.,* 1999).

Among all CDRM catalysts, Co based catalysts are preferred in CDRM due to their high activity, wide availability and low cost of the metal (Wang *et al.,* 2001). Cobalt has two crystal structures; close-packed hexagonal (hcp) and face-centered cubic (fcc). Both phases can coexist at room temperature; however, the fcc structure is thermodynamically

preferred above 450°C and the hcp phase is favored at lower temperatures (Dinego *et al.,* 1999). Since high temperatures up to 1073K are required for CDRM, fcc structure of cobalt is widely preferred in computational studies (Rodrígunez-Ramos *et al.,* 1998).

The aim of this thesis is to analyze CDRM reaction and the behaviours of its reactants, products and some intermediate products on the cobalt surfaces. Density functional theory (DFT) calculations have been utilized on Co(111) surface in order to analyze electronic interaction between the absorbates and active centers, for finding the energetically most stable configuration of the adsorbates and the CDRM surface reaction. Firstly adsorption behaviours of all reactants (CO_2, CH_4), some products and intermediate products (CO, O, CH_3) of CDRM were investigated. Then, transition stage (TS) searches of CH_4 dehydrogenation and CO formation were carried out to obtain the reaction pathways and activation energies of elementary steps. At the end, C+O and CO+CH_3 coadsorptions were performed on Co(111) and the effect of surface coverage on coadsorption of C+O were analyzed with different C and O concentrations on Co(111).

Chapter 2 contains a detailed literature survey on the theoretical background of CDRM as well as the catalysts involved in the process. Chapter 3 presents the background of DFT and the computational methodology used in this study. The results obtained are presented and discussed in Chapter 4; whereas Chapter 5 consists of the conclusions of the present study and recommendations for future work.

2. LITERATURE SURVEY

Production of energy through the use of cleaner, safer and more economical and efficient has been very attractive research subject due to the increasing demands of energy and increasing concerns on the climate change. Hydrogen is an important energy carrier for industrial processes and it can be produced from fossil fuels such as methane or renewable resources such as methanol. Natural gas, containing high amount of methane, is an important and widely used hydrogen source in industry (Dadyburjor *et al.,* 2009).

2.1. Carbon Dioxide Reforming of Methane

The rising emissions of greenhouse gasses in atmosphere have become major environmental problems leading to global climate change and this problem heightened the interest worldwide for the control, conversion and utilization of green house gases (Yang *et al.,* 2010). Carbon dioxide reforming of methane (CDRM), Equation (2.1), consumes two thermodynamically stable greenhouse gasses and helps avoiding global warming and decreasing the emission of CO_2; therefore CDRM can be beneficial to environment (Özkara-Aydınoğlu *et al.,* 2009). CDRM produces synthesis gas, which is a mixture of carbon monoxide and hydrogen, a valuable mixture for the chemical and petrochemical industry.

Carbon dioxide reforming of methane (CDRM): $CH_4 + CO_2 \rightarrow 2CO + 2H_2$ (2.1)

The history of CDRM is not very old. Steam reforming of methane, Equation (2.2), has been dominantly used by the industry in hydrogen and syngas production. However in recent years, the important advantages of CDRM over steam reforming of methane have been realized and CDRM has become a hot research area. One of the important advantages of CDRM over methane steam reforming and partial oxidation is its lower H_2/CO product ratio (Liu *et al.,* 2006).

Steam reforming of methane: $CH_4+H_2O\leftrightarrow 3H_2+CO$ (2.2)

Partial oxidation: $CH_4+0.5O_2\leftrightarrow 2H_2+CO$ (2.3)

CDRM produces syngas having H_2/CO in 1/1 ratio which is suitable for further production of valuable hydrocarbons and oxygenated compounds through following reactions such as Fischer-Tropsch process, methanol synthesis, dimethyether synthesis or ammonia synthesis (Özkara-Aydınoğlu *et al.,* 2009). In other words, CDRM is a possible way to obtain syngas with high purity. Another advantage of CDRM is that it can be employed in areas where water is not available (Huang *et al.,* 2010). Additionally, CDRM allows the use of natural gas resources with high CO_2 content, avoiding the expensive and intricate gas separation process. Biogas, a renewable resource containing methane (40-70%) and carbon dioxide (30-60%) produced by anaerobic digestion of biomass is also a raw material of CDRM process (Román-Martínez *et al.,* 2009).

CDRM have become a good alternative process to methane steam reforming and partial oxidation of methane that have several difficulties such as the high operation and equipment costs. CH_4 and CO_2 are relatively inexpensive due to their natural abundance; hence, conversion of these two molecules to higher-value compounds is of great interest. Keulen and co-workers studied comparative cost analysis of the production of acetic acid using three processes (steam reforming, partial oxidation and CDRM) and reported that that the operative cost of CDRM is lower than those of the other two processes (Scelza *et al.,* 2005; Bradford *et al.,* 1999).

CDRM process can be used with different purposes, such as a system for solar energy transfer to chemical energy, energy storage in the form of CO and H_2. Additionally CDRM is preferred reaction for chemical energy transmission systems due to desirable thermodynamic properties such as large heat of reaction and reversibility (CETS) (Gallego *et al.,* 2008a).

The most important disadvantage of CDRM is the required high temperatures to reach high conversion levels due to highly endothermic nature of the process. This requirement results in deactivation of catalysts by coke deposition, and sintering of the metallic phase and support. Coke is formed mainly by two reactions, methane decomposition and carbon monoxide disproportionation (Boudouard reaction). In addition

to these undesired side reactions, the reverse water gas shift reaction, CO and CO_2 methanation reactions, coke gasification reaction and steam reforming reaction may accompany CDRM as side reactions (Gallego *et al.,* 2008b). Some side reactions of CDRM are (Gallego *et al.,* 2008b):

Reverse water gas shift: $H_2+CO_2 \leftrightarrow CO+H_2O$ (2.4)

CO_2 methanation: $CO_2+4H_2 \leftrightarrow CH_4+2H_2O$ (2.5)

CO methanation: $CO+3H_2 \leftrightarrow CH_4+H_2O$ (2.6)

Steam reforming: $CH_4+2H_2O \leftrightarrow CO+3H_2$ (2.7)

Boudouard reaction: $2CO \leftrightarrow C+CO_2$ (2.8)

Methane decomposition: $CH_4 \leftrightarrow C+2H_2$ (2.9)

Coke gasification: $C+H_2O \leftrightarrow CO+H_2$ (2.10)

Methane decomposition is an endothermic reaction and favored at higher temperatures and lower pressures, whereas carbon monoxide disproportionation is exothermic and favored at lower temperatures and higher pressures (Nagaoka *et al.,* 2001).

2.2. Reaction Mechanism of CDRM

Many mechanisms regarding CDRM reaction have been proposed for 44 years using different techniques and catalysts. By assuming that replacing steam by carbon dioxide has no significant impact on the reforming mechanism, early studies proposed a reaction mechanism for CDRM using the results of methane steam reforming (Bradford *et al.,* 1999).

Rostrupnielsen and Bak-Hansen proposed a reaction mechanism over some transition metals, Ni, Ru, Rh, Pd, Ir, and Pt, which began with the dissociative adsorption of

methane. They reported that, as a second step, surface carbon was oxidized by surface oxygen. It was indicated that surface oxygen came from the dissociative adsorption of CO_2 (Rostrupnielsen *et al.,* 1993).

$$C^*+O^* \rightarrow CO^*+^* \quad (2.11)$$

Erdohelyi *et al.,* Efstathiou *et al.,* and Wei and Iglesia proposed similar pathways, however Mark and Maier proposed a reaction mechanism that is different in CO_2 adsorption step. They reported that dissociatively adsorbed methane produced surface carbon that reacted with gas-phase CO_2 to produce CO (Sullivana *et al.,* 2010).

$$C^*+CO_2 \rightarrow 2CO+^* \quad (2.12)$$

Erdöhelyi and co-workers suggested that CO_2 adsorption was dissociative in nature verified by the presence of adsorbed CO-band signals in their IR studies. However, Bradford and Albert Vannice reported that CO_2 adsorption was nondissociative because in-situ DRIFTS experiments showed the bands representing carbonates (Erdohelyi *et al.,* 1993; Bradford *et al.,* 1999).

In recent years, Maestri *et al.* proposed a different reaction pathway on Rh/Al_2O_3 with C_1 micro kinetic model which claimed that the oxidation of surface carbon occurred through reaction with adsorbed hydroxyl. It was concluded that the reaction of adsorbed CO_2 and dissociatively adsorbed H_2 produced adsorbed hydroxyl (Sullivana *et al.,* 2010):

$$C^*+OH^* \rightarrow CO^*+H^* \quad (2.13)$$

$$CO_2^*+H^* \rightarrow CO^*+OH^* \quad (2.14)$$

As a reaction pathway of CDRM using Rh supported on strontium-substituted hexaaluminate, Sullivan *et al.* proposed a reaction mechanism, for which CH_4 and CO_2 are adsorbed onto the catalyst surface first. Secondly, the surface-adsorbed CH_4^* undergoes a series of methane dehydrogenation steps; at the end, adsorbed atomic hydrogen H* and carbon C* are formed. The adsorbed CO_2^* dissociates to O* and CO* and surface C* and

O* produce CO*. Then CO* reacts with H* and produces HCO*. After the HCO* dissociates to O* and CH*, O* and CH* participate regenerates C*, H*, and CO*. Ultimately, recombinative desorption of H* produces gas-phase H_2 and CO* produces gas phase CO by desorption (Sullivana *et al.,* 2010).

Osaki and co-workers studied surface reaction analysis of CDRM on various supported Ni catalysts, and they proposed that adsorbed CH_4 dehydrogenated over metal producing surface C and H_2. Stevens and Chuang proposed reaction mechanism over Rh/Al_2O_3 using combined in situ infrared spectroscopic and mass spectrometric study and reported that CH_4 was decomposed into CH_x species and H_2 (Osaki *et al.,* 1994; Chuang *et al.,* 2004).

Jiao *et al.* investigated reaction pathways of CDRM on Ni(111) by using DFT with CASTEP. The simplified mechanism was proposed on the basis of computed energy barriers. The first reaction is CO_2 dissociation into surface CO and O ($CO_2 \rightarrow CO + O$) and sequential dissociation of CH_4 into surface as CH and H ($CH_4 \rightarrow CH_3 \rightarrow CH_2 \rightarrow CH$). The second reaction is CH oxygenation into CHO ($CH + O \rightarrow CHO$), which is more favored than CH dissociation into C and hydrogen ($CH \rightarrow C + H$). The third reaction is the dissociation of CHO into surface CO and H ($CHO \rightarrow CO + H$). At the end, H_2 and CO desorb from Ni and form free H_2 and CO. This article revealed that the rate-determining step is the dissociative adsorption of CH_4, and the key intermediate is surface adsorbed CHO (Jiao *et al.,* 2006). Zhu *et al.* used DFT via VASP to investigate the reaction mechanism of CDRM on Ni(111). In their work, the most energetically favorable adsorption configurations of the species were obtained, and the transition states for all the possible elementary steps were reported. According to the results presented, CO_2 dissociates into CO and O via a direct pathway. O is seen to be the primary oxidant of CH_x intermediates. By using this information, two reaction pathways are constructed through CH and C. According to proposed pathways by Zhu *et al.*, CO_2 and CH_4 dissociation is followed by the oxidation of the produced CH and C by O to produce CHO and CO; and then CHO decomposes to CO and H_2. Zhu *et al.* revealed that as for these two reaction pathways, the oxidation step was predicted to determine the overall reaction rate (Zhu *et al.,* 2009). Moreover, the CH_4 dissociation was revealed to be the rate-limiting step at lower temperatures by Özkara-Aydınoğlu (Özkara-Aydınoğlu *et al.,* 2010).

Kinetic study of CDRM on Co-Ni/Al_2O_3 and Ce-Co-Ni/Al_2O_3 catalysts was performed by Adesina and co-workers. They proposed a dual-site Langmuir-Hinshelwood mechanism that involves methane dehydrogenation producing surface C and H_2 and CO_2 disruption producing CO and surface O; and then O transfer to the metal sites cleaning of C with the O (Adesina *et al.,* 2010).

2.3. Catalysts for CDRM

The performance of CDRM process heavily depends on activity, selectivity and stability specs of its catalyst. The major factors that affect the performance of CDRM catalysts are type(s) of the metal(s) used in catalyst preparation, type of the support, addition of promoters and the conditions used in catalyst preparation and pretreatment. Various kinds of catalysts have been studied in order to reach high activity, selectivity and stability. Most of the catalysts studied are Ni, Co, Rh, Pd, Pt, Ir, Fe and Cu based. The most used support types are ZrO_2, Al_2O_3, MgO, ZrO_2-La_2O_3, La_2O_3, SiO_2, TiO_2, $ZnOCeO_2$-ZrO_2 and CeO_2 (Bradford *et al.,* 1999).

Bradfordand Vannice studied CDRM on group VIII metals supported on different kinds of oxides. In their study, the observed order of activity was: Rh> Ru > Ir > Ni, Pt, Pd > Co > Fe, Cu. They indicated that differences in activity for CDRM over a given metal dispersed on different supports may result from metal-support interactions and/or the participation of O or OH species from the support in the metal-support interfacial region. They mentioned that the catalysts were deactivated by coke deposition; however, noble metals had less tendency of deactivation (Bradford *et al.,* 1999).

According to results reported by Román-Martínez and co-workers, the most active catalysts for CDRM are catalysts based on VIII, IX and X group metals, especially Rh, Ru and Pt. However, these catalysts are not promising for this process at industrial use because these metals are expensive and of limited availability. For that reason, other metals like Ni and Co that have proper activity, availability and price are mostly used at industrial level. Actually, Ni and Co have been extensively studied as catalysts for CDRM. The main disadvantage of Co and Ni catalysts is their deactivation by coke deposition as the reaction progresses (Román-Martínez *et al.,* 2009).

The effect of support (SiO_2, Al_2O_3, MgO, and TiO_2) on catalytic behavior of Ru catalysts for the CH_4/CO_2 reforming was investigated by various research groups. Nagaoka and co-workers reported that Ru/TiO_2, showing a low coking extent, was a suitable catalyst (Nagaoka *et al.,* 2001). Wang and co-workers studied CDRM over the supported Rh catalysts. Two kinds of oxides, reducible (CeO_2, Nb_2O_5, Ta_2O_5, TiO_2, and ZrO_2) and irreducible (γ-Al_2O_3, La_2O_3, MgO, SiO_2, and Y_2O_3) oxides were used as the supports. According to this research, MgO and γ-Al_2O_3 were found as the most desirable supports since they lead to a high and stable activity. Additionally, ZrO_2 and CeO_2 have a very long activation period (Wang *et al.,* 2000).

Kwak and co-workers studied CDRM with Ni catalysts supported on Al_2O_3 and MgO-Al_2O_3 with core/shell structures. These catalysts were synthesized under multi bubble sonoluminescnce conditions and it was reported that these catalysts yielded a good conversion rate of 92% at 800°C and exhibited good thermal stability for the first 150h. It was revealed that supported Ni catalysts, $Ni/Al_2O_3$and Ni/MgO-Al_2O_3, with core/shell structures showed good activity and thermal stability in all types of CDRM reactions. The Boudouard reaction, methane decomposition, and their reverse reactions alternately occurred during CDRM process with Ni/Al_2O_3 and Ni/MgO-Al_2O_3 catalysts so that the activity or thermal stability of the catalysts was not influenced by fixed amounts of carbon deposited on the surfaces of catalysts. This study concluded that these supported Ni catalysts with core/shell structure had great potential in fuel processing (Kwak *et al.,* 2011).

CDRM reaction of a series of carbon-based nickel catalysts has been investigated by Menéndez and co-workers. In their study, the surface chemistry of carbons used as supports, the drying method and the temperature of the reduction stage were considered as the parameters that may affect the Ni particle size, Ni dispersion and final catalytic activity of the samples in CDRM. The oxidation of the carbon support was found favoring the interaction between Ni particles and carbon surface, and therefore Ni dispersion. It was revealed that the reduction temperature also had a great effect on the Ni particle size. The use of microwave drying rather than conventional drying exhibited significant advantages in the preparation of carbon-supported Ni catalysts: the operating time was greatly reduced, smaller Ni particle sizes were obtained and the influence of the surface chemistry

on the Ni particle size was minimized. On the other hand, for the specific application of these catalysts to CDRM, neither an improvement in Ni particle size nor Ni dispersion was found to be essential due to the sintering of Ni particles that took place at the reaction temperature (800°C). The oxidation of the carbon support was also found an important factor on the catalytic activity of Ni-based catalysts (Menéndez *et al.,* 2010).

CDRM over Ni/ZrO_2-CeO_2 catalysts was investigated by Papadopoulou et al. and Montoya et al. According to the paper of Papadopoulou et al, zirconium enhances the textural properties of the CeO_2-ZrO_2 supports and the corresponding catalysts. Moreover, zirconium improves the textural stability under thermal reductive treatment. Additionally, an important increase in the reducibility of both supports and catalysts was observed in the presence of Zr. It was revealed that the zirconium-rich catalyst exhibited higher activity and the higher resistance to the formation of carbon deposits (Papadopoulou *et al.,* 2010). In the article of Montoya et al., they reported that ZrO_2 stability increased with an increase in CeO_2 concentration. Moreover, it was indicated that the catalyst activity was increased with the CeO_2 content, although some degree of deactivation, caused by the sintering of the support, was not completely prevented by ceria addition. The addition of Ce to the ZrO_2 support caused no decrease in conversion levels and led to a significant enhancement in the stability. It was concluded that the catalysts containing ceria increased catalytic reactivity and improved the performance of the catalysts (Montoya *et al.,* 2000).

Özkara-Aydınoğlu et al. revealed that there was a great influence of the impregnation strategy and the Ce amount on the activity and stability of the Ce promoted Pt/ZrO_2 catalysts in CDRM. According to their results, Ce promoted Pt/ZrO_2 catalyst, which was prepared by co-impregnation method, showed the highest catalytic activity and stability. This high activity was caused by the intensive interaction between Pt and Ce phases for co-impregnated sample. Strong and extensive Pt-Ce surface interaction caused an increase in the number of Ce^{3+} sites and improved the dispersion of Pt. When temperature increased, conversion and H_2/CO ratio increased. The reported results revealed that ZrO_2 is an important and very effective support for CDRM, and addition of Ce to the catalyst increases activity of the catalyst (Özkara-Aydınoğlu *et al.,* 2009).

2.3.1. Co-based Catalysts

Recent studies have shown that Co based catalysts are preferred in CDRM due to their high activity, wide availability and low cost of the metal (Wang *et al.,* 2001).

2.3.1.1. Experimental Studies. Ji and co-workers investigated the effect of preparation methods on the performance of Co based catalysts for CDRM through comparing three cobalt-based catalysts having the same cobalt content; a catalyst prepared by conventional impregnation on commercial γ-Al_2O_3 support (CoAlCO-IM), a sol-gel-made catalyst on γ-Al_2O_3 (CoAlSG-IM) and a catalyst prepared by direct sol-gel processing from organometallic compounds (CoAlSG).All three catalysts had the same catalytic activity at 750°C. However, CoAlSG catalyst showed relatively low catalytic activity at low reaction temperatures (550-650°C), high space velocity and it had the best coking resistivity. Fast and heavy coke deposition occurred on CoAlCO-IM catalyst. Compared to CoAlCO-IM catalyst, CoAlSG had stronger metal-support interaction, smaller metallic Co particles and richer surface OH species. It was concluded that all of these properties may help the inhibition of coke formation (Ji *et al.,* 2001).

Yamada and co-workers conducted a study about strontium carbonate supported cobalt catalyst for CDRM under pressure. In their study, catalytic performance of Co-SrO catalysts, which were prepared by oxalate co-precipitation method or citric acid method showed a steady activity. Additionally, cobalt supported on strontium carbonate prepared by impregnation method (Co/$SrCO_3$) exhibited the comparable activity with high tolerance to oxidative atmosphere under reaction conditions (Yamada *et al.,* 2004).

In another study conducted by Wang and his co-workers**,** the optimization of cobalt loading of the Al_2O_3 supported catalyst for CDRM was investigated. It was found that the stability of Co/γ-Al_2O_3 catalysts was strongly dependent on the Co loading and calcination temperature. For some loading levels (6 wt% for T_c=500°C and 9 wt% for T_c=1000°C), stable activities were obtained. However, for high Co loadings (>12 wt%), notable amounts of carbon were deposited over the catalysts during CDRM**,** and catalyst deactivation was observed **(**Wang *et al.,* 2002).

Influences of the addition of trace amounts of Pt or Ru and of replacement of Co by Ni on CDRM performance have been investigated for TiO_2 supported samples. The addition of noble metals improved the catalytic stability of Co/TiO_2, and noble metals enhanced the reducibility of cobalt oxide. The strong resistance of Co/TiO_2 to coke deposition was also retained by the catalysts. The replacement of Co by a small amount of Ni also enhanced the catalytic stability; however, replacement by an excessive amount of Ni caused the decrease of catalytic stability due to coking (Nagaoka *et al.,* 2004).

Bimetallic CDRM catalysts were studied by Román-Martínez *et al.* and Takanabe *et al.* carried out a study on Ni, Co and bimetallic Ni-Co catalysts for CDRM. They revealed that the catalysts with the highest cobalt content were the most active and stable ones, but these catalysts produced a large amount of carbon. The higher activity achieved by cobalt rich catalysts was related with the higher activity of this metal for methane decomposition. However, their high stability was caused by the presence of large particles involved in long-term stable conversion owing to the fact that they produced non-deactivating carbon deposits (Román-Martínez *et al.,* 2009). Takanabe and co-workers investigated titania-supported cobalt and nickel bimetallic catalysts for CDRM. Bimetallic $Co\text{-}Ni/TiO_2$ catalysts with an appropriate Co/Ni ratio exhibited high and stable activities without carbon deposition. Nevertheless, the monometallic Co/TiO_2 catalyst deactivated rapidly due to the oxidation of metal. This research concluded that the advantages of the bimetallic catalysts were high resistance to undesirable metal oxidation and coking (Takanabe *et al.,* 2005).

In order to achieve high levels of methane and carbon dioxide conversions with minimized carbonaceous deposits, Ruckenstein *et al.* And Mondal *et al.* investigated the effect of support on the Co catalysts. Ruckenstein and co-workers studied on CDRM over the performance of Co supported on an alkaline earth metal oxide (MgO, CaO, SrO or BaO) and also on $\gamma\text{-}Al_2O_3$ and on SiO_2. It was shown that only MgO has lead to a high and stable activity among these supports. $\gamma\text{-}Al_2O_3$ gave initially a high CO yield, but its activity was decayed rapidly. All the other supports led to low CO yields. In addition, CaO and SiO_2 had low stabilities (Ruckenstein *et al.,* 2000). Mondal and co-workers worked on CDRM over supported CoO_x (accompanied with MgO, ZrO_2 or CeO_2) catalysts. In that

study, the sequence of catalyst activities in terms of their supports was found in the following order: $MgO>ZrO_2> CeO_2>Y_2O_3>ThO_2$ **(**Mondal *et al.,* 2007).

Considering the fact that Co based catalysts have high activity, wide availabilities, low costs and ZrO_2 has good activity, stability and coke resistance; Aksoylu et al. investigated the effect of addition of metal additives, namely lanthanum, cerium, manganese, potassium and magnesium on CDRM activity of Co/ZrO_2 catalyst. It was revealed that the most important factors which primarily determine activity are dispersion properties and the type of the promoter. The observed order of methane conversions over promoted cobalt catalysts in terms of the type of promoters added is Ce>none>La≈Mn>Mo>K>Mg. The highest activity was obtained with Ce-doped Co/ZrO_2 catalyst and this catalyst had a very limited activity loss. The presence of Ce on the surface produces an additional storage capacity for oxygen coming from ZrO_2 support; it goes through continuous reduction/oxidation cycle producing mobile surface oxygen, and improves the oxygen transfer. Thus, Ce makes the catalyst more resistant to carbon deposition. Unpromoted Co catalyst is reported to have high activity at the beginning of the reaction, but it lost 40% of its initial CH_4 activity because its resistance to coke deposition is poor. La-modified catalyst had high stability, moderate activity and it caused no significant amount of coke deposition. La-promoted catalyst had less amount of deposited carbon than either the Ce-promoted or the unpromoted ZrO_2 catalyst. Consequently, Co-Ce and Co-La catalysts were found more promising Co based CDRM catalysts than the other samples (Özkara-Aydınoğlu *et al.,* 2010).

Effects of Ce/Zr ratio on the structure and performances of $Co\text{-}Ce_{1-x}Zr_xO_2$ catalysts for CDRM were investigated by Chu et al. Several advantages of the $Co\text{-}Ce_{0.8}Zr_{0.2}O_2$ catalyst in CDRM reaction were reported. The sample reducibility was improved by charge effect of cubic $Co\text{-}Ce_{0.8}Zr_{0.2}O_2$ with CoO_x species. The catalyst with cubic phase was reported having smaller nano crystallite sizes of Co_3O_4 than that of the other catalysts having tetragonal and mixed phases. The decrease of cobalt size in $Co\text{-}Ce_{0.8}Zr_{0.2}O_2$ catalyst avoided carbon deposition and decreased the content of C_β which caused the catalyst deactivation. This research concluded that the cubic $Co\text{-}Ce_{0.8}Zr_{0.2}O_2$catalyst gave rise to the lower apparent activation energy and showed a higher activity and stability in CDRM reaction (Chu *et al.,* 2010).

Huang and co-workers studied the effect of cobalt content on the catalytic performance of molybdenum carbides in CDRM. They revealed that incorporating cobalt into the Mo_2C structure at a Co/Mo ratio of 0.4, i.e. a $Co_{0.4}Mo_1C_x$ catalyst, gave higher activity and stability than those of Mo_2C catalysts, but higher molar ratios decreased the promoting effect and facilitated the phase separation of the promoter (Huang *et al.,* 2010).

The effect of temperature on the structure and performance of Co-W-C catalyst for CDRM was investigated using both performance tests and near-edge X-ray absorption fine structure (NEXAFS) spectroscopy. For Co-W-C, CDRM reactivity was greatly improved after being exposed to methane at 850°C. To obtain reasonable reactivity for CDRM, Co-W oxide must be reduced, and the active stable catalysts must contain large amounts of carbon that was formed at or near the surface region. This species can play a critical role in the reactivity and stability of the catalysts for CDRM (Dadyburjor *et al.,* 2009).

2.3.1.2. Computational Studies. Cobalt has two crystal structures-close-packed hexagonal (hcp) and face-centered cubic (fcc). Both phases can coexist at room temperature; however the fcc structure is thermodynamically preferred above 450°C and the hcp phase is favored at lower temperatures (Dinego *et al.,* 1999). Since the thermodynamic limitations make it necessary to increase the temperature up to 1073K for CDRM, fcc structure of cobalt is widely preferred in computational studies concerning CDRM (Rodrígunez-Ramos *et al.,* 1998).X-ray diffraction (XRD) characterization also verified that Co(111) is the main surface of the metallic fcc cobalt (Huang *et al.,* 2010).

Huang et al. studied the dehydrogenation of CH_4 on the Co(111) surface using density functional theory calculation (DFT). After obtaining the adsorption energies of all the species involved in the dehydrogenation from CH_4 to C, each elementary step was calculated on the Co(111) surface (Huang *et al.,* 2010):

$$CH_4^* \rightarrow CH_3^* + H^* \rightarrow CH_2^* + 2H^* \rightarrow CH^* + 3H^* \rightarrow C^* + 4H^* \quad (2.15)$$

According to their results, CH_4 was dissociated to CH_3 and then formed to CH_2 and CH through sequential dehydrogenation. Additionally, CH_3 and H prefered to adsorb on 3-fold hollow hcp and fcc sites, and CH_2, CH and C prefered to adsorb on hcp sites. The

adsorption energies of CH_x (x=0-4) and H adsorption exhibited the order: CH_4<CH_3<H<CH_2<CH<C. By evaluating the computed energy barriers of the elementary steps along the most favorable reaction pathway, CH_4 activation into CH_3 and H was found the rate-determining step on the Co(111) surface, in agreement with the experimental results. It was concluded that CH_2 was quite unstable on Co(111) surface and CH dehydrogenation into C and H was difficult (Huang *et al.,* 2010).

The regular CO overlayers at coverage h=1/3 adsorbed on the (0001) surface of hcp Co and (111) surface of fcc Co were studied by first-principles density-functional theory with the exchange-correlation component in the PBE form. In this research, adsorption in atop, bridge, and three-fold hcp or fcc position were investigated. Additionally, the adsorption energies, CO stretching frequencies, geometry, work function, and local magnetic moments were evaluated. It was revealed that the recently proposed correction to adsorption energy of CO favored the atop adsorption site; however the remaining sites were almost degenerate in energy. This study showed that the CO molecule lowered magnetization on neighbouring Co atoms, and the effect decreased with the increase in coordination of adsorption site. Nevertheless, this trend was not the result of the different C–Co separation at different adsorption sites. The results indicated that a very small magnetic moment appeared on CO couples antiferromagnetically to Co. Most results were found very similar for the Co(0001) and Co(111) surfaces (Pick *et al.,* 2007).

The influence of different exchange and correlation functionals on the site preference for CO adsorption on Co(0001) surface was carried out through using density functional theory (DFT) calculations by Zu and co-workers. In their work, the results of all functionals identified atop and hollow sites as the favored sites with degenerate energy. Additionally, almost identical adsorption geometries and vibrational frequencies were obtained for CO adsorption in each high symmetry site. By using empirical correction to adsorption energy, atop site was uniquely identified as the most favorable site, in perfect agreement with experimental results. This study provided another correct site preference with empirical correction to adsorption energy (Zu *et al.,* 2008).

O'Shea and co-workers carried out periodic density functional calculations to study the interaction of CO_2 with slab models representing the low index surfaces of Co(fcc).

They predicted that the interaction is structure sensitive and that the molecular structure of CO_2 on the Co(100) and Co(110) faces is highly distorted and reminiscent of CO_2^-. This is defined as spontaneous activation of the adsorbed molecule. Additionally, it was indicated that Co(100) and Co(110) oriented surfaces of the Co(fcc) nanoparticlesin supported catalysts were likely to trigger CO_2 activation and hence to ease CO_2 dissociation which is in agreement with recent experimental observations (O'Shea *et al.,*2008).

Possible intermediates in the formation of carbon deposits on H_{fcc}-Co(111) were investigated by using DFT by Steen and co-workers. The results exhibited that graphene could be formed as stable, smaller carbon clusters on the flat Co surface beginning from adsorbed atomic carbon. It was revealed that the preferential adsorption site of atomic carbon was the hcp-site. As a result of the reduced metal-carbon interaction and carbon-carbon interaction on the tertiary carbon atom, the formation of linear carbon structures is slightly favored over the formation of branched carbon structures with the same number of carbon atoms. Sequential addition of atomic carbon was proposed as the initial step for the formation of carbon overlayers causing the formation of (branched) carbon chains. It was observed that linkage of carbon chains at high coverage would result in the formation of the more stable aromatic clusters and further growth of these structures would result in the formation of graphene on the surface. It was concluded that a prerequisite for this mechanism was a relative high mobility of adsorbed atomic carbon, which could be expected on flat surfaces and low coverage (Steen *et al.,* 2008).

2.3.2. Deactivation of Catalysts

Catalyst deactivation means loss of activity with time and it is inevitable, but it can be slowed or prevented, and some of its consequences can be avoided. Catalyst deactivation has chemical, physical and thermal aspects that are very important for the design of deactivation-resistant catalysts, the operation of industrial chemical reactors, and the study of specific reactivating procedures (Forzatti *et al.,* 1999).

The mechanisms of catalyst deactivation can be classified into six intrinsic mechanisms of catalyst decay: poisoning, fouling or coking, sintering, vapor compound formation accompanied by transport, attrition/crushing, vapor-solid and solid-solid

reactions. Poisoning, vapor formation, vapor-solid and solid-solid reactions are chemical mechanisms; thermal degradation and sintering are thermal mechanisms; and fouling, attrition and crushing are mechanical mechanisms. Poisoning is the strong chemisorption of reactants, products or impurities on sites otherwise available for catalysis. Vapor formation is the reaction of gas with catalyst phase to produce volatile compound; however, vapor-solid and solid-solid reactions are the reactions of fluid, support, or promoter with catalytic phase to produce inactive phase. Attrition and crushing are the loss of catalytic material due to abrasion and the loss of internal surface area due to mechanical-induced crushing of the catalyst particle (Bartholomew *et al.,* 2001).

For CDRM reaction, catalyst deactivation is mainly caused by coking and sintering. Sintering means the loss of active surface via structural modification of the catalyst. This type of deactivation is a physical and generally thermally activated process. Sintering of the CDRM catalysts can be avoided through the use of thermally resistant supports and/or catalysts having promoters stabilizing the metal (Bartholomew *et. al.,* 2001).

Side reactions of CDRM occur on the catalyst surface leading to the formation of carbonaceous residues which is usually referred to as coke or carbon. Coke physically covers the active centers and causes catalyst deactivation. Coke is produced by the following reactions (San-José-Alonso *et al.,* 2009):

Methane decomposition: $CH_4 \rightarrow C + 2H_2 \quad \Delta H=+17.9$ kcal/mol (2.16)

Boudouard reaction: $2CO \rightarrow C + CO_2 \quad \Delta H=-41.2$ kcal/mol (2.17)

Coke deposits may amount to 15% or even 20% (w/w) of the catalyst; therefore they may deactivate the catalyst by pore blocking and covering of the active sites. Carbonaceous deposition is dependent on the operating conditions, the physicochemical properties of the catalysts, like the types of the active metal, the grain size of the active metal, types of support and promoter, etc. The amounts of coke deposited into the catalyst pores may be determined by burning the coke with air, by monitoring the evolution of the combustion products CO_2 and H_2O and measuring the weight changes via TG-DTA techniques (Forzatti *et al.,* 1999).

The coke profile is very non-uniform when preferential deposition of carbon occurs in the exterior of the particle. The non-uniform coke deposition inside the catalyst pores may be explained by the existence of intraparticle diffusional limitation. When coke accumulates within the catalyst pores, the effective diameter of the pores decreases and therefore the resistance to the transport of reactants and products increases in the pores. If coke is concentrated near the pore mouth, coke will be more effective as a barrier than the same amount uniformly distributed on the pore wall, and finally pore blockage can take place (Forzatti *et al.,* 1999).

The coke deposition may be controlled to a certain extent by using an optimal catalyst composition and an appropriate combination of process conditions. Coke can be avoided by designing catalysts which will increase surface carbon-oxygen interaction through the use of suitable support and promoter combinations (San-José-Alonso *et al.,* 2009). When equilibrium is reached between the rate of coke production and the rate of coke removal during the reaction, steady-state conditions are reached and therefore a certain level of coke present on the catalyst surface. If the rate of coke deposition is higher than that of coke removal, a suitable regeneration is necessary (Forzatti *et al.,* 1999).

The studies about CDRM have been extensively conducted on supported group VIII metal catalysts. It is reported that both noble metals (e.g. Ru, Rh, Pd, Pt, Ir) and non-noble metals were catalytically active towards this reaction. One of the important advantages of the noble metal as a CDRM catalyst is that they exhibit activity with low carbon deposition; however, noble metal catalysts have some disadvantages like their high cost and limited availability. On the contrary, non-noble metals are less expensive and widely available. On the other hand, CDRM is strongly endothermic process requiring high temperatures (typically 800-900°C) which may lead to a rapid deactivation of the catalyst by carbon deposition and/or metal sintering for non-noble metals when the active metals are incorporated/impregnated into conventional supports such as Al_2O_3, SiO_2,MgO (Yang *et al.,* 2010).

Several investigations have been conducted to compare noble metals with Ni catalysts for CDRM. According to results, an important improvement in catalytic activity and stability was obtained by adding Pt, Pd and Rh to a $Ni_{0.03}Mg_{0.97}O$ catalyst. Over SiO_2

supported Ni-Rh catalysts, the effective formation of a Ni-Rh alloy can occur, but only the Rh-rich catalysts were resistant against deactivation and coke deposition. Ni_Y and Ni_β monometallic catalysts were found almost inactive in comparison with zeolite supported Pt and Pt-Ni catalysts. A significant effect on the catalytic performance was observed as Ru was added to supported Ni catalysts. By alloying Au into Ni surface layer, the supported Ni catalyst was more robust; implying the presence of Au atoms at low-coordination sites blocked the adsorption of C atoms, and thus significantly avoids the formation of carbon whiskers (Yang *et al.,* 2010).

In terms of thermodynamics standpoint, operating the CDRM at high temperatures and with CO_2/CH_4 ratios far above unity is suggested to avoid regions having a thermodynamic potential for carbon formation. Nevertheless, from an industrial point of view, operating at lower temperatures with CO_2/CH_4 ratios around unity is preferred. Several studies have been carried out on the development of CDRM catalysts through incorporating kinetic inhibition of carbon formation under conditions where deposition is thermodynamically favorable. Although noble metal catalysts have been found to be less sensitive for carbon formation, Ni catalyst is still to be preferred due to their much lower cost. Various methods have been suggested to avoid the carbon formation on Ni catalysts. Sulfur passivation, alkaline or alkaline earth metal promoters and using Ni-Mg solid solution catalyst are some examples of these methods. The carbon deposition-gasification treatment was also proposed as a method for minimizing carbon formation (Chen *et al.,* 2001).

Therdthianwong et al. investigated improvement of Ni/Al_2O_3 catalyst stability and coke resistance by ZrO_2 addition. A series of Ni/Al_2O_3 catalysts were prepared by incipient to wetness impregnation method. It was seen that the main reason of the deactivation of Ni/Al_2O_3 was coke deposition and this deactivation was inhibited by ZrO_2. According to results, The $Ni/ZrO_2/Al_2O_3$ co-impregnated catalyst revealed a higher BET surface area and catalytic activity than those of the sequentially impregnated catalysts. Nevertheless, coke inhibition capability of the promoted catalysts prepared by each of two methods was similar. The results showed that when ZrO_2 was added, the stability of Ni/Al_2O_3catalyst was greatly improved in terms of coke inhibition through enhancing the dissociation of oxygen intermediates. These intermediates then reacted with carbonaceous species

deposited over the metal. The results indicated that the desired carbon-oxygen interaction was achieved for carbon removal (Therdthianwong *et al.,* 2008).

The study Ni, Co and bimetallic Ni-Co catalysts for the CDRM was carried out by Román-Martínez and co-workers. This study showed that the most active and stable catalysts were Co(9) and NiCo(1-8) catalysts with the highest cobalt content for CDRM; however, an important disadvantage of these catalyst is the large amount of carbon formation. It is revealed that the reason of the higher activity by cobalt rich catalysts can be the higher activity of this metal for methane decomposition, which is the rate limiting step of the overall reaction. This high stability of the Co rich catalysts was found to be related with the presence of large particles that are involved in long-term conversion since they formed non-deactivating carbon deposits. It is concluded that Co rich catalysts exhibited good catalytic properties but they should be improved to minimize carbon deposition (Román-Martínez *et al.,* 2009).

Effect of MgO additive on catalytic properties of Co/SiO_2 in CDRM was studied by Mirodatos and co-workers. It was observed that adding magnesia to a Co/silica catalyst had a very positive effect on catalyst stability arise from the formation of a magnesium silicate phase, which can be only obtained for a tuned amount of MgO addition. The first effect was explained through prevention of cobalt phase sintering by limiting particle coalescence, which was the main sintering process under these reacting conditions. As a second positive effect, the specific medium basicity of the silicate adlayer allowed a reversible storage of a pool of hydrogeno-carbonates in the vicinity of Co particles, ensuring a constant feed in surface oxygen and therefore the immediate oxidation of surface carbide produced from methane cracking into carbon monoxide. It is concluded that this bi-functional process minimized deactivating carbon formation by limiting formation of bulk cobalt carbide and, therefore, formation of carbon filament, which may cause reactor plugging and/or particle fragmentation; and by suppressing encapsulating carbon formation, which limits access of reactant to the active cobalt phase (Mirodatos *et al.,* 2004).

3. METHODOLOGY

3.1. Theory behind Computational Methods: Quantum Chemical Models

Theoretical models have been developed to calculate molecular structure and energetics. These models have generally been classified into two categories; quantum chemical models and molecular mechanics models.

Quantum chemical models originate from the Schrödinger equation. According to this equation, molecules are defined as collections of nuclei and electrons, without any reference to chemical bonds, and the solution is obtained in terms of the motions of electrons with approximations. Quantum chemical models differ on the basis of the nature of these approximations.

Hartree-Fock approximation is one of the approximations and it provides the foundation of Hartree-Fock molecular orbital model. This approximation assumes that electrons move essentially as independent particles without interaction. This model can be based on complete description of electron correlation. In reality, the electrons are further away from each other than predicted by this approximation; so two approaches have been developed for the improvement of Hartree-Fock model;

- First approach is to develop a more flexible description of electron motions for ground and excited states and some models are constructed. Most commonly used models are Configuration interaction (CI) and Møller-Plesset (MP) models. The second-order Møller-Plesset model (MP2) is the most practical and extensively used model.

- The second approach is to use an additional explicit term to account for the way in which electron motions affect each other. This approach is based on an exact solution for idealized system and it is developed using empirical parameters. Density functional model is constructed for this account (Hehre, 2003).

3.1.1. Schrödinger Equation

All quantum mechanical methods ultimately stems from the Schrödinger equation, which introduced for the special case of hydrogen atom is as follows:

$$\left[-\frac{1}{2}\nabla^2 - \frac{Z}{r}\right]\psi(r) = E\psi(r) \tag{3.1}$$

Here, the quantity in square brackets represents the kinetic and potential energy of an electron at a distance r from a nucleus of charge Z. E is the electronic energy, and ψ, a function of the electron coordinates, r, is a wave function describing the motion of the electron Wave functions for the hydrogen atom are the familiar s, p, d... atomic orbitals (Hehre, 2003).

3.1.2. Many-body Problem

The Schrödinger equation is modified for a multinuclear, multi electron system as follows:

$$\hat{\mathrm{H}}\psi = E\psi \tag{3.2}$$

Here, ψ is a many-electron wave function and $\hat{\mathrm{H}}$ is the so-called Hamiltonian operator.

The many-electron Schrödinger equation cannot be solved exactly, therefore approximations are developed to provide practical methods. The first one of them is Born-Oppenheimer approximation. According to this approximation, the motion of nuclei is slow compared to the electrons because of large difference in mass; thus it is assumed the nuclei do not move (Hehre, 2003).

To allow total-energy calculations to be performed accurately and efficiently, further simplifications can be introduced. These include density-functional theory to model the electron-electron interactions, pseudopotential theory to model the electron-ion

interactions, the use of supercells to model systems with periodic geometries, and iterative minimization techniques to relax the electronic coordinates (Payne *et al.,* 1992).

3.1.3. Electron-electron Interactions

The most difficult problem in any electronic structure calculation is the need to take the effects of the electron-electron interactions into account. Most first-principles approaches recast the problem from the one where electron interactions are explicit to the one where the interactions are represented by an effective potential acting on apparently independent electrons.

An early approach was developed by Hartree. The missing point in the Hartree approach is that it neglects the exchange and correlation effects. Hartree-Fock approach treats the exchange interaction properly; however, the method remains inherently approximate since it neglects the correlation (Payne *et al.,* 1992).

3.1.3.1. Density Functional Models. DFT is one of the approaches to the treatment of the electron correlation. DFT is *"ab-initio"* in the sense that it is derived from first-principles and does not require adjustable parameters. Its advantages are: (i) DFT includes both exchange and correlation effects (ii) DFT is not as computationally demanding as the other ab-initio methods, such as CI or MP2 (Hehre, 2003).

Density functional models have at their heart the electron density, as opposed to the many electron wave function, ψ (r_1, r_2,...). Hohenberg and Kohn proved that the total energy, including exchange and correlation, of a electron gas is a unique functional of the electron density. If the true exchange-correlation functional can be used, DFT theoretically would give the exact solution, however the exact exchange-correlation functional required for this purpose is unknown. The minimum value of the total-energy functional is the ground-state energy of the system, and the density that yields this minimum value is the exact single-particle ground-state density (Payne *et al.,* 1992). Kohn and Sham then extended the theory to practice by showing how the energy can be partitioned into kinetic energy, potential energy and electron-electron repulsion terms and showed how it is

possible, formally, to replace the many-electron problem by exactly equivalent set of self-consistent one-electron equations (Hohenberg *et al.,* 1964).

The energy is written as:

$$E = E_T + E_V + E_J + E_{XC} \tag{3.3}$$

Here, E_j is the Hartree Coulomb term for electron-electron interaction, which does not include exchange and correlation effects and E_v is the electron-nuclear interaction energy. The electron energy is given by E_T, E_{XC} is the exchange and correlation energy. Except from E_T, all others depend on the total electron density, ρ(r) (Hehre, 2003).

$$\rho(r) = 2\sum_i^{orbitals}\left|\psi_{i(r)}\right|^2 \tag{3.4}$$

Here ψ_i are the so-called Kohn-Sham orbitals and the summation is carried over pairs of electrons (Hehre, 2003).

Within a finite basis set, the energy components may be written as follows:

$$E_T = \sum_\mu^{basis}\sum_\nu^{functions}\int {}_\mu(r)\left[-\frac{1}{2}\nabla^2\right]{}_\nu(r)dr \tag{3.5}$$

$$E_V = \sum_\mu^{basis}\sum_\nu^{functions} P_{\mu\nu}\sum_A^{nuclei}\int {}_\mu(r)\left|\frac{Z_A}{r-R_A}\right|{}_\nu(r)dr \tag{3.6}$$

$$E_{XC} = \frac{1}{2}\sum_\mu\sum_\nu^{basis}\sum_\lambda^{functions}\sum_\sigma P_{\mu\nu}P_{\lambda\sigma}(\mu\nu|\lambda\sigma) \tag{3.7}$$

$$E_{xc} = \int f(\rho(r), \nabla\rho(r), \ldots)dr \tag{3.8}$$

Z is the nuclear charge, r is the distance between the nucleus and the electron, P is the density matrix, (μν|λσ) are two-electron integrals and f is an exchange/correlation functional, which depends on the electron density and perhaps as well the gradient of the density (Hehre, 2003).

The minimum value of the Kohn-Sham energy functional is equal to the ground state of the energy system of electrons. Minimizing E with respect to the unknown orbital coefficients yields a set of matrix equations, the "Kohn-Sham equations". In the Kohn-Sham equations, the effective potential is the Kohn-Sham potential (Payne *et al.,* 1992).

The set of wave functions that minimize the Kohn-Sham energy functional are given by self-consistent solutions to the Kohn-Sham equations. The Kohn-Sham equations must be solved self-consistantly so that the occupied electronic states generate a charge density that produces the electronic potential that was used to construct equations (Payne *et al.,* 1992).

E_{XC} handles the complexity of interacting electrons and finding E_{xc} remains the great challenge in DFT. There are two major approximations to solve this problem. The most widely used is the local-density approximation (LDA), which was introduced by Kohn and Sham along with Kohn-Sham equations. The LDA states that E_{xc} can be given by assuming that the exchange-correlation energy is that of a uniform electron gas of density $\rho=\rho(r)$ (Payne *et al.,* 1992). Then,

$$E_{xc=} \int dr\rho(r)\varepsilon_{xc}\,(\rho(r)) \tag{3.9}$$

where $\varepsilon_{xc}(\rho)$ is the exchange-correlation energy per electron in a uniform gas of density ρ. However in reality, the charge density is highly non-uniform around the atoms. Functionals that have been developed that include dependence o the gradient of the density are called generalized-gradient approximation (GGA).

3.1.4. Periodic Supercells

The supercell approximation is used to deal with two difficulties: an infinite number of electrons in the system each for which a wave function must be calculated, and since each electronic wave function extends over entire solid, an infinite basis set is required to expand each wave function. These problems can be handled by carrying out calculations on periodic systems and applying Bloch's theorem to the electronic wave functions (Payne *et al.,* 1992).

3.1.5. Bloch's Theorem

Bloch's theorem states that in a periodic system each electronic wave function can be written as a product of a cell-periodic part (f term) and wavelike part (exponential part) that contains wave vector k, and this theorem gives an important advantage of imposing periodic boundary conditions.

$$\psi_i(r) = exp[ik.r]\, f_i(r) \tag{3.10}$$

The cell periodic part can be expanded using a basis set consisting of a discrete set of plane waves whose wave vectors are reciprocal lattice vectors of crystal. Therefore each electronic wave function can be written as a sum of plane waves (Payne *et al.,* 1992).

3.1.6. K-point Sampling

Electronic states are allowed only at a set of k-points determined by the boundary conditions that apply to the bulk solid. The density of allowed k points is proportional to the volume of the solid. The infinite numbers of electrons in the solid are accounted for by infinite number of k points, and only a finite number of electronic states are occupied at each k point. The Bloch theorem deals with the difficulty of calculating an infinite number of electronic wave functions to one of calculating a finite number of wave functions at an infinite number of k-points. The occupied states at each k-point contribute to the electronic potential, thus in principle an infinite number of calculations are needed. Nevertheless, the electronic wave functions at k-points that are very close together will be almost identical. Therefore, it is possible to represent the electronic wave functions over a region of k space by the wave functions at a single k point. This suggests that DFT expressions that contain a sum over k-points can be efficiently evaluated using a numerical scheme that performs summation over a small number of special points in the Brillouin zone. Additionally, symmetry considerations show that only k-points within the irreducible segment of the Brillouin zone should be taken into account (Payne *et al.,* 1992)

3.1.7. Plane-Wave Basis Set

Bloch's theorem states that the electronic wave functions at each k-point can be expanded in terms of a discrete plane-wave basis set. In principle, an infinite number of plane waves are required for such an expansion. However, the coefficients, $C_{i,k+G}$, for the plane waves with small kinetic energy, $(1/2)|k+G|^2$, are more important than those with large kinetic energies. Thus, the plane wave basis set can be truncated to include only plane waves that have kinetic energies that are smaller than some particular cutoff energy. If a continuum of plane-wave basis states were required to expand each electronic wave function, the basis set would be infinitely large no matter how small the cut-off energy is. Application of the Bloch theorem allows the electronic wave functions to be expanded in terms of a discrete set of plane waves. Introduction of an energy cutoff to the discrete plane-wave basis set produces a finite basis set.

3.1.8. Plane-Wave Representation of Kohn-Sham Equations

When plane waves are used as a basis set for the electronic wave functions, the Kohn-Sham equations assume a particularly simple form.

$$\sum_G \left[\frac{1}{2}|k+G|^2\delta_{GG'} + V_{ion}(G-G') + V_H(G-G')+V_{XC}(G-G')\right] c_{i,k+G} = \varepsilon_i c_{i,k+G} \qquad (3.11)$$

In this form, the kinetic energy is diagonal, and the various potentials such as electron-ion, Hartree, exchange-correlation are described in terms of their Fourier transforms (Payne *et al.,* 1992).

Other advantages of the plane wave basis sets are to provide efficient geometry optimization and molecular dynamics schemes owing to the ease of calculating derivatives of the total energy with respect to atomic displacements and to improve convergence of plane-wave basis set calculations because of the systematic way of adding more basis functions.

3.1.9. Electron-Ion Interactions (Pseudopotential Theory)

The most important drawback of plane waves is the slow convergence due to the Coulomb singularities and the rapidly changing density because of the inner electrons. A very large number of plane waves are needed to expand the tightly bound core orbitals and to follow the rapid oscillations of the wave functions of the valance electrons in the core region. The pseudopotential approximation allows the electronic wave functions to be expanded using a much smaller number of plane-wave basis set.

It is well known that physical properties of solids are dependent on the valance electrons to a much greater extent than on the core electrons. Pseudopotential theory allows one to replace the strong electron ion potential with a much weaker potential - pseudopotential - that describes all the salient features of a valance electron moving through the solid, including relativistic effects. Thus, the original solid is now replaced by pseudo valance electrons and pseudo-ion cores. These pseudoelectrons experience exactly the same potential outside the core region. The fact that the potential is weaker is crucial, however, because it makes the solution of the Schrödinger equation much simpler by allowing expansion of the wave functions in a relatively small set of plane waves.

3.2. Material Studio Software

3.2.1. MS Visualizer

In this study, DFT calculations were performed in a repeated slab geometry. Periodic boundary conditions produce a pair of two-dimensionally infinite surfaces that are separated by a substantial slab of material in one direction and on the other by a vacuum region. This is carried out by Material Studio (MS) of Accelarys Inc. The core product of MS is the Material Visualizer. It constructs and manipulates graphical models of molecules, surfaces and layered structures.

In order to construct a surface, firstly the bulk structure of the material is optimized. The bulk crystal structure of a material can be obtained by importing from MS library if the material is monometallic, or by preparing manually depending on the experimental data

if database does not include crystal structure of insert. In this study the bulk structure of cobalt was imported from the database of MS library. The ball-and-stick model is given in Figure 3.1.

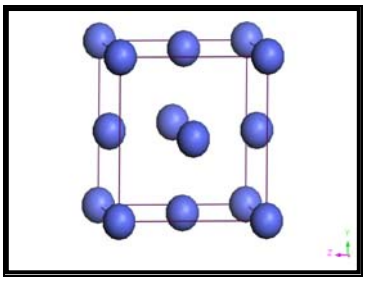

Figure 3.1. The Co unit cell. Blue balls represent Co atoms.

Secondly, slab is built hence surface is created by cleaving and inserting vacuum (Figure 3.2). Cleaving is done by entering the Miller indices of the surface into the specific dialog box and then, specifying the depth of the slab, that is the number of atomic layers in the slab. After cleaving, the thickness of the slab that is the separation of the two surfaces is determined. To guarantee that there is not any attraction between the surface and the bottom of the following slab in z-direction, the slab has to include a sufficiently thick vacuum layer above the surface. Nevertheless, since the computational time increases with increase of the slab thickness, the appropriate values must be carefully chosen. In order to keep the computational time at the minimum, the atoms of the bottom layers are generally kept at their bulk positions while those in the surface layers of the slab are relaxed.

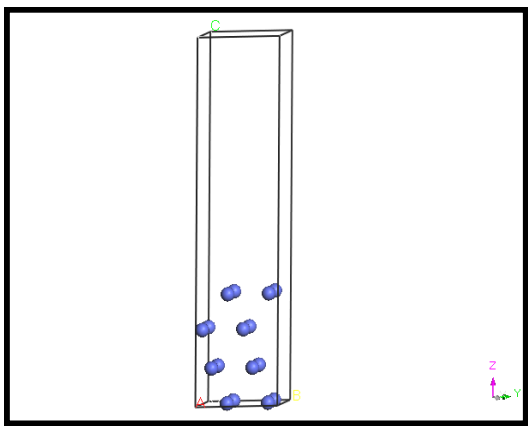

Figure 3.2. The side view of p(2x2) surface unit cell of Co(111).

MS Visualizer is integrated with special DFT codes, like CASTEP and DMol3, for energy calculations. The total energy of a molecule or a crystal refers to the energy of a specific arrangement of atoms. The zero of the energy is taken to be the infinite separation of all electrons and nuclei, so the total energy is generally negative.

3.2.2. MS CASTEP

CASTEP is a first principles quantum mechanics based program for performing electronic structure calculations. Within the density functional formalism it can be used to simulate a wide range of materials especially solid state materials. CASTEP employs a total energy plane-wave pseudopotential method. In the mathematical model of the material, it replaces ionic potentials with effective potentials acting only on the valence electrons in the system. Electronic wave functions are expanded through a plane-wave basis set, and exchange and correlation effects in electron-electron interactions can be included within either LDA or GGA approximations. CASTEP uses pseudopotentials and plane wave basis sets together to calculate the forces on the atoms easily. This enables efficient optimization of ionic configurations of molecules, solids, and interfaces. Electronic relaxation is carried out with density mixing algorithm, by default (Clark *et al.,* 2005).

3.2.3. MS DMol3

DMol3 is a modeling program that uses density functional theory (DFT) to simulate chemical processes and predict properties of materials in MS. DMol3 uses localized numerical orbitals for the basis functions and each function corresponds to an atomic orbital. The basis functionals are expressed numerically as values on atomic centered spherical-polar mesh, rather than analytical Gaussian orbitals. The angular portion of each function is the appropriate spherical harmonic and the radial portion is achieved by solving the atomic DFT equations numerically. The possible optimization algorithms are not under user control and the possible one is determined automatically depending on the system under study (Delly *et al.,* 1990; Delly *et al.,* 2000).

DMol3 is a fast and useful algorithm and it is widely used in transition state search. During the chemical reaction, the energy increases to a maximum and then decreases to the energy of the products. The maximum energy along the reaction pathway is called as the activation energy and the structure obtained at this energy level is called transition state (TS).

In this study, synchronous transit methods that interpolate a reaction pathway were used for locating the TS in DMol3. In this method, firstly Linear Synchronous Transit (LST)/Optimization calculation (Figure 3.3) was carried out by a single interpolation to a maximum energy. Hence, an idealized set of structures connecting reactant and product was obtained by linearly interpolating the distances between pairs of atoms in the reactant and product.

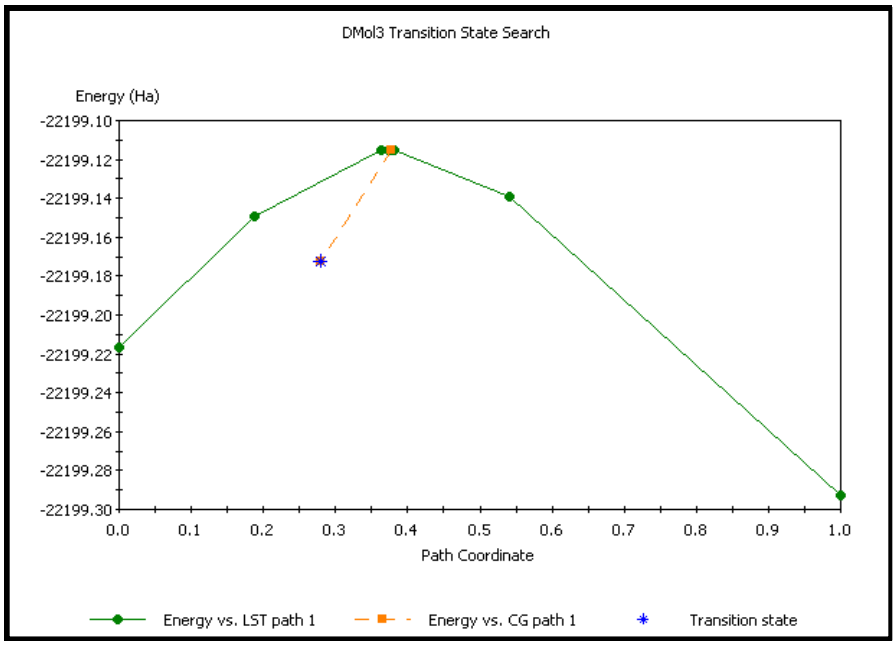

Figure 3.3. A sample energy curve obtained fater LST algorithm.

3.3. Parameters for Optimization

During the DFT calculations with CASTEP and DMol3, sampling of the Brillouin zones were obtained by summation over Monkhorst-Pack meches of dimensions 4x4x1 on a (2x2) cell and modified according to the changes in slab dimensions. Exchange and

correlation were included by using GGA along with the Perdew-Burke-Ernzerhof (PBE) functional.

In CASTEP, electron-ion interaction was included through the use of ultra soft pseudopotentials. A smearing range of 0.1 eV was used at the Fermi level. Pulay's density mixing scheme was used for the self-consistent field (SCF) electronic minimization. The convergence criteria for the structure optimizations were 2.0 x 10^{-6} eV/atom for SCF, 1.0 x 10^{-5} eV/atom for energy, 0.05 eV/Å for maximum force, and 2.0 x 10^{-3} Å for maximum displacement.

In DMol3 TS searches are performed with "All Electron (AE)" method to treat core electrons. AE provides no special treatment of cores and all electrons are included in the calculation. In this calculations double-numeric quality basis set, DNP, which includes d-polarization function is used. A Fermi smearing of 0.01 Hartree (Ha) was used. The smearing option allows the fractional orbital occupancy and improves SCF convergence. During the TS calculations, the geometry optimization convergence threshold for the rms forces on the atoms was 0.05 Ha/Å.

3.4. Calculating the Properties

3.4.1. LDOS Charts

Local density of states represents a useful semi-qualitative tool for analyzing the electronic structure. LDOS shows which atoms in the system contribute electronic states to various parts of the energy spectrum.

LDOS calculation itself can be carried out using either Gaussian smearing or linear interpolation. CASTEP uses a simplified linear interpolation scheme for LDOS calculations. This method is based on linear interpolation in paralelopipeds formed by the points of the Monkhorst-Pack set, followed by the histogram sampling of the resultant set of band energies. Charts are obtained by plotting the LDOS data (electron/eV) versus energy (eV). (MS CASTEP, 2001)

3.4.2. Mulliken Charges

In DMol3, basis set superposition effects are minimized by dissociation of molecules accurately to their constituent atoms. However, in CASTEP no information is obtained regarding the localization of the electrons in the system because of the delocalized nature of the electrons in the system. In CASTEP, population analysis is carried out using a projection of the plane wave states onto a localized basis. In both codes, the resulting states are then used to provide the atomic populations with a technique performed using the Mulliken formalism. In the Mulliken analysis, the charge is determined for a given atom A by,

$$Q(A) = \sum_k w_k \sum_\mu^{onA} \sum_\nu P_{\mu\nu}(k) S_{\nu\mu}(k) \tag{3.12}$$

where S and P are the overlap and population matrices, respectively and they are indicated as,

$$S_{\nu\mu}(k) = \langle \varphi_\mu(k) | \varphi_\nu(k) \rangle \tag{3.13}$$

$$P_{\nu\mu}(k) = \langle \varphi^\mu(k) | \rho(k) | \varphi^\nu(k) \rangle \tag{3.14}$$

and w is the weight associated with the k-points in the Brillouin zone (Segall *et al.,*1996).

4. RESULTS AND DISCUSSION

The aim of this study is to analyze the adsorption and reaction steps of CDRM reaction on the cobalt (111) surface by using DFT calculations. In this context, the adsorption/coadsorption of reactants, reaction intermediates, and the reaction between them was studied. Local Density of State analysis allowing understanding the electronic interaction between the metal atoms of the sites and the adsorbate molecules was also used whenever detailed analysis is necessary.

Firstly adsorption behaviours of all reactants (CO_2, CH_4), some products and intermediate products (CO, O, CH_3) of CDRM were investigated. After LDOS profiles corresponding to these adsorptions were obtained, adsorption strengths of them were evaluated according to adsorption energies, bond lengths and LDOS profiles. Elementary steps of the dehydrogenation from CH_4 up to C+H and CO formation reaction from C and O coadsorption were studied on Co(111) surface with transition stage (TS) searches to understand how this processes occur. Additionally, the changes in the behavior of C and O with different surface coverages were analyzed by using different initial structures in coadsorption. Lastly, CO and CH_3 coadsoptions were carried out to evaluate their behaviors through coadsorptions.

4.1. Calculational Parameters

Spin-polarized density functional theory calculations, as implemented in the program package CASTEP and DMol3 in Materials Studio of Accelrys Inc. (version 5.0), were carried out in repeated slab geometry. The surfaces were modeled as four-layer slabs and all layers were allowed to relax out of plane together with the absorbate until all the relevant atomic forces were below threshold. Cells were modified by making 2x2 supercell with 14 Å vacuum thickness. In this study, Monkhorst-Pack special k-point sets were used for Brillouin zone integrations. 4x4x1 k-point sampling was determined as optimum k-point sampling after the comparative accuracy analysis of the k-point sampling was performed with 4x4x1, 6x6x1 and 8x8x1. It was seen that the energy result difference between 4x4x4 and 8x8x1 was below 0.04 eV for Co bulk geometry optimization.

Surface energies, adsorption energies and LDOS charts were obtained with CASTEP, whereas DMol3 was used for analyzing the TS searches. In CASTEP calculations, exchange and correlation were included through the use of generalized gradient approximation (GGA) along with the Perdew-Burke-Ernzerhof (PBE) functional. Pulay's density mixing scheme was used for the SCF electronic minimization. However, in DMol3 local density approximation (LDA) and the Perdew-Wang (PWC) functional were used. In CASTEP calculations, 340 eV cutoff value was used after the accuracy of the cutoff value was comparatively analyzed based on the results obtained with 300, 330, 340 and 360 eV cutoff values. It was seen that the energy result difference between 340 eV and 360 eV was negligible, 0.0108 eV, compared to the ones between 330 eV and 340 eV, 0.0159 eV and the ones between 300eV and 330eV, 0.1826 eV for Co bulk geometry optimization. In DMol3, a real-space cutoff of 5.0 Å was used.

Since Co(111) surface is the main surface of metallic fcc cobalt (Huang *et al.,* 2004) and it has been widely studied in other computational and experimental works, Co single crystal surface was modeled by the (111) termination (Huang *et al.,* 2010; Pick*et al*., 2007; Methfessel *et al.,* 2009). Additionally, in order to determine the top layer position in cleaving, energy comparison was carried out, and it was seen that energy sensitivity of top layer position was ±0.0005 eV. The slab was cleaved with 1.0 top layer as the most favorable top layer position. Throughout the study, the slab dimensions were kept unchanged.

In order to analyze the adsorption step of the CDRM reaction on Co surface, energy and geometry optimizations were performed for CO_2, CH_4, CH_3, CO and O adsorptions, as well as C+O and CH_3+CO coadsorptions. Adsorption energies were calculated by

$$E_{ads} = E^{slab+adsorbate} - E^{slab} - E^{adsorbate} \tag{4.1}$$

LDOS calculations were directly performed by using CASTEP. In order to analyze the change of LDOS profiles of Co atoms, the effect of the site type was considered. If substrate was adsorbed on atop site, the interaction between substrate and Co atom affects only this Co atom; however, if substrate was adsorbed on fcc site, the interaction between substrate and four Co atoms affects all four Co atoms. Therefore the change of LDOS

profiles of one of the fcc substrate-coordinated Co atoms was recorded as a result of %25 of substrate-Co atoms interaction.

4.2. CO_2 Adsorption on Co(111)

The strengths of CO_2 adsorptions on the possible sites at a constant surface coverage of 0.25 ML were analyzed. To simulate this surface coverage, one CO_2 molecule was placed in a (2×2) unit cell (Figure 4.1). The CO_2 adsorption energies on these four sites, i.e. top (T), bridge (B), hollow hcp (H_{hcp}) and hollow fcc (H_{fcc}) are reported in Table 4.1.

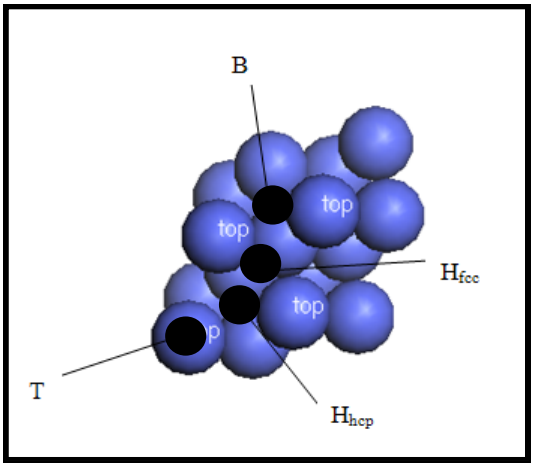

Figure 4.1. Ball model of Co(111) and various CO_2 adsorption sites available on the surface. Sites are labeled as T (atop), B (bridge), H_{hcp} (hollow hcp) and H_{fcc} (hollow fcc).

As can be understood from the calculated adsorption energies of CO_2 on Co(111), the CO_2 adsorption on all sites are very weak. Among these possible adsorption sites, H_{hcp} is the most favorable site with the highest adsorption energy, -0.0592 eV. Negative E_{ads} values are obtained CO_2 adsorptions on H_{hcp} and H_{fcc} sites; however these values, -0.0244 eV and -0.0592 eV are very close to zero. The reason of these low adsorption energies is that high amount of energy was spent for the configurational change of CO_2 molecule led by its interaction with the surface. The important difference between LDOS profiles of bare and coordinated C atom of CO_2 proves that there is a significant electronic interaction between CO_2 molecule and the surface. The highest occupied molecular orbital (HOMO) of free CO_2 is $1\pi_g$, and the lowest unoccupied molecular orbital (LUMO) is $2\pi_u$. LUMO is situated at ca. 8 eV and HOMO is situated at ca. -3 eV in the LDOS profile of free CO_2.

Upon chemisorption, the 2 π_u and 1 π_g bands shifted downward, to ca. -7 eV and -10 eV, respectively, and adsorbed $CO_2$was stabilized on H_{hcp} and H_{fcc} sites as indicated by the energy profiles in Figure 4.2-a and Figure 4.2-b. The orbitals of bare CO_2 which interact particularly with the metal d bands produce peaks below the Fermi level and these peaks were shifted downward with smaller amplitude for CO_2-Co coordinated case as seen on these LDOS profiles. In other words, there is a significant decrease in electron density around carbon in the corresponding energy levels after chemisorptions. The following site has stable CO_2 adsorption in terms of the adsorption strength is bridge site, and there is no significant adsorption energy difference between fcc site and bridge site; the results indicate that adsorption of CO_2 on bridge site is weak but stable. Although the adsorption energy calculated is positive and higher than that of the adsorption on bridge site, there is also an interaction between the coordinated Co atom and the CO_2 molecule for atop adsorption as indicated by Figure 4.2-c. There, the LDOS of metal d–band showed a downward shift in energy accompanied by both e^- loss around Fermi level, and e^- density increase around ca. -4 eV and for the energy range -7 eV to -4 eV. The optimized geometry of the CO_2-Co system indicate that even for the atop adsorption the CO_2 molecule did not leave the site but move slightly far away from the surface.

Table 4.1. Energy of CO_2 adsorption on Co(111). The values correspond to total adsorption energy per unit cell. The distance of C from the nearest Co atom is exhibited as d(Co-C).

Site	**E_{ads} (CO_2) (eV)**	**$d_{C\text{-}Co}$ (Å)**
T	0.3522	1.8440
H_{fcc}	-0.0244	2.2470
B	0.0428	2.0540
H_{hcp}	-0.0592	1.8840

The molecular linearity of CO_2 was distorted through the adsorptions of CO_2 on all sites; however the most significant change in O-C-O bond angle was recorded on the CO_2 adsorption on H_{hcp} site (Figure 4.3). Additionally, CO_2 was bended towards the Co surface through the adsorptions on H_{hcp} and H_{fcc} sites

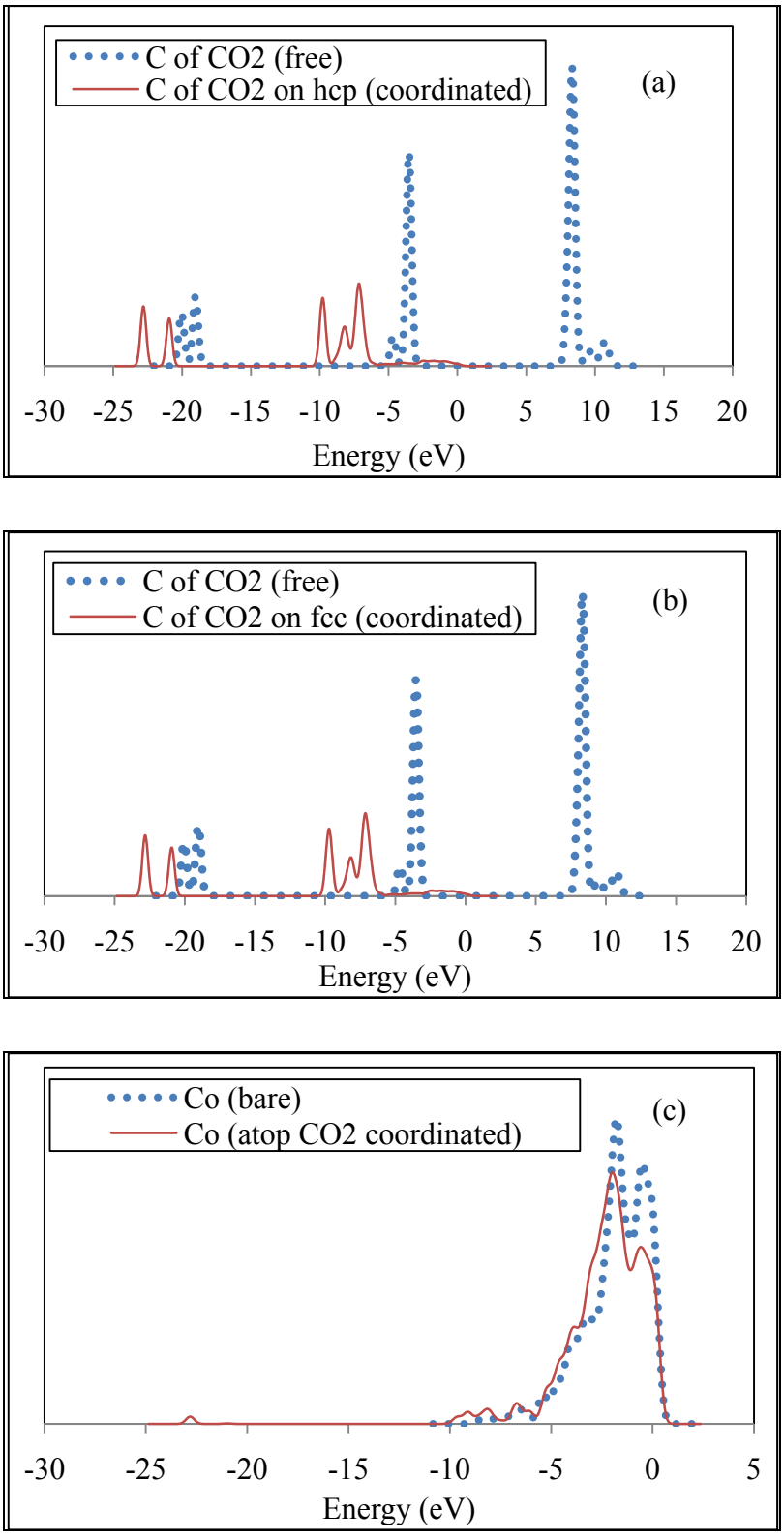

Figure 4.2. Changes in LDOS (a) C of adsorbed CO_2 molecule on H_{hcp} site (b) C of adsorbed CO_2 molecule on H_{fcc} site (c) atop CO_2-coordinated Co atom at 0.25 ML.

The results presented in the previous studies are consistent with the current ones; for example O'Shea *et al.* carried out DFT calculations for the interaction of CO_2 with the fcc Co(111) using periodic slab models and they revealed that geometry optimization leads to two stable structures as hcp and bridge sites (O'Shea *et al.,* 2008).

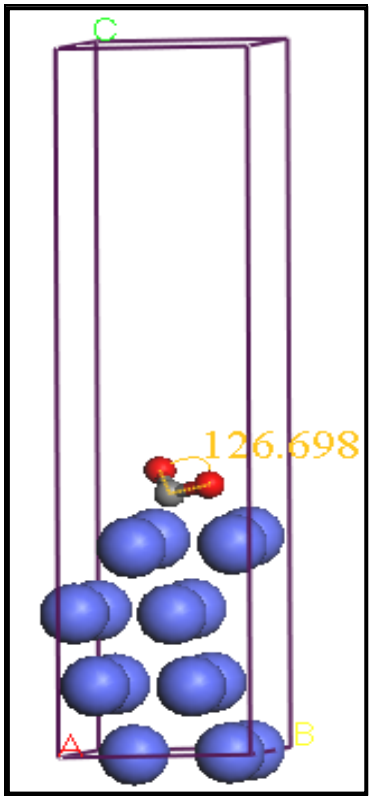

Figure 4.3. CO_2 adsorption on H_{hcp} site at 0.25 ML.

4.3. CH_4 Adsorption on Co(111)

The strengths of CH_4 adsorptions on the possible sites at a constant surface coverage of 0.25 ML were analyzed. In order to simulate this surface coverage, one CH_4 molecule was placed on a (2×2) unit cell (Figure 4.1). CH_4 adsorption energies on these four sites, i.e. top (T), bridge (B), hollow hcp (H_{hcp}) and hollow fcc (H_{fcc}) are reported in Table 4.2.

The strengths of the CH_4 adsorptions on all possible sites of Co(111) are very low in terms of the calculated adsorption energies; thus, further analysis is needed for understanding whether the adsorption is stable. Among the possible adsorption site, negative E_{ads} values were obtained for CH_4 adsorptions on atop and H_{fcc} sites; however

these values, -0.0341 eV and -0.0059 eV are very close to zero. Upon energy optimization performed for each of the CH_4-coordinated sites, the geometry of the CH_4-Co systems show that CH_4 dissociated to CH_3 and H molecules for atop and bridge sites; this means that CH_3+H was more stable than CH_4 on atop and bridge sites of Co(111). In other words, CH_4 adsorption was not stable on atop and bridge sites, in spite of negative E_{ads} value of CH_4 adsorption on atop site. It should be noted that unstability of CH_4 adsorption on bridge site is also indicated by a high positive E_{ads} value, 0.1373 eV.

Table 4.2. Energy of CH_4 adsorption on Co(111). The values correspond to total adsorption energy per unit cell. The distance of C from the nearest Co atom is exhibited as d(Co-C).

Site	**E_{ads} (CH_4) (eV)**	**$d_{C\text{-}Co}$ (Å)**
T	-0.0341	2.049
H_{fcc}	-0.0059	3.9120
B	0.1373	2.2000
H_{hcp}	0.0018	3.6420

After simulation of CH_4 on H_{fcc} and H_{hcp} sites, the shape of the CH_4 molecule was preserved but the distance of C from the nearest Co atom was increased. These results indicate that CH_4 was adsorbed on H_{fcc} and H_{hcp} sites either very weakly or the adsorption is unstable. For further analysis, LDOS profiles of the CH_4-coordinated Co atoms were analyzed; the insignificant change in the electron density profile of the Co d-band for both sites supports the unstability option. The LDOS profiles of coordinated and free Co atom for hcp site are given in Figure 4.4 as an example. This results is parallel to the results of the study by Huang *et al.;* they concluded that the interaction of CH_4 and Co(111) surface was very weak and CH_4 was favored to dissociate to CH_3. In their study, adsorption energies of CH_4 on all sites were found almost the same and the change of adsorption energies is very small about 0.01 eV. It is known that DFT might not provide an accurate description of van der Waals type weak binding states. Due to such limitations, Huang *et al*. did not attempted further characterization of CH_4 adsorption on a special surface (Huang *et al.,* 2010).

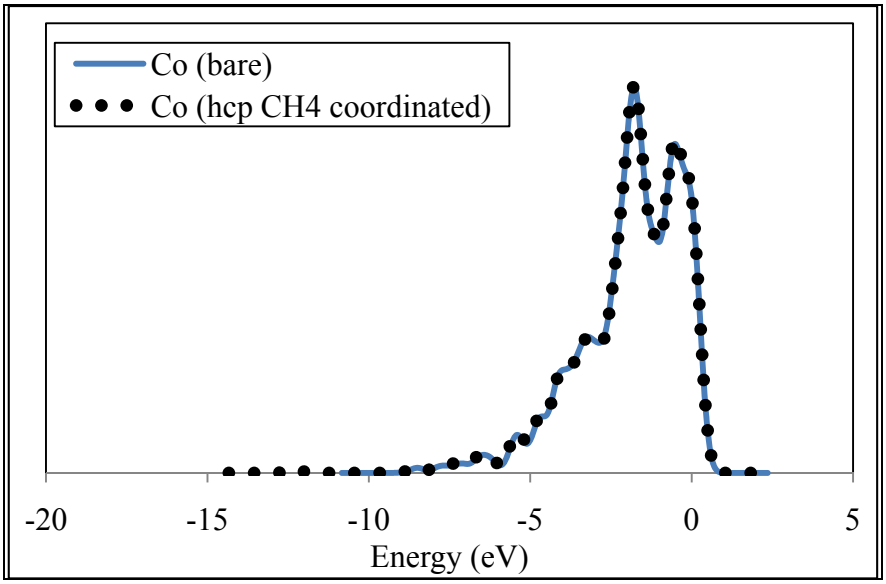

Figure 4.4. Changes in LDOS atop CH_4-coordinated Co atom at 0.25 ML.

4.4. CH_3 Adsorption on Co(111)

The strengths of CH_3 adsorptions on the possible sites at a constant surface coverage of 0.25 ML were analyzed. In order to simulate this surface coverage, one CH_3 molecule was placed on a (2×2) unit cell (Figure 4.1). The CH_3 adsorption energies on these four sites, i.e. top (T), bridge (B), hollow hcp (H_{hcp}) and hollow fcc (H_{fcc}) are reported in Table 4.3.

Table 4.3. Energy of CH_3 adsorption on Co(111). The values correspond to total adsorption energy per unit cell. The distance of C from the nearest Co atom is exhibited as d(Co-C).

Site	E_{ads} (CH_3) (eV)	$d_{C\text{-}Co}$ (Å)
T	-2.3719	1.9860
H_{fcc}	-2.6129	2.7060
B	-2.8887	2.0850
H_{hcp}	-2.8588	2.0550

As indicated by the highly negative E_{ads} values calculated, the CH_3 adsorption is stable on all Co(111) sites, except on the bridge site, and the adsorption is strong. Although the highest CH_3 adsorption energy was obtained on bridge site, which was almost same as

the adsorption energy of CH_3 on the H_{hcp} site; as CH_3 initially placed in bridge position assumed hcp position upon energy optimization, the adsorption on bridge site is unstable. As a consequence, the H_{hcp} site can be assumed to have highest adsorption stability which is supported by the shortest C-CO distances obtained for that site. The lowest E_{ads} was obtained for atop site. It should be also noted that the E_{ads} change is within ±0.24 eV for all four sites. The bond lengths between CH_3 and nearest Co atom were almost the same for all sites. The average bond length between CH_3 and nearest Co atom was obtained as 2.202 Å.

Similar results were obtained by Huang *et al.* with DFT calculations and Huang *et al.* concluded that CH_3 adsorption on Co(111) is energy favored and the energy preference of CH_3 adsorption is 3-fold hollow site; the greater the exothermic adsorption energies are considered as the indication of more stable the adsorption models. According to their results; CH_3 interacts with one Co atom forming Co-C bond at the top site, and the C-H bond is slightly larger than that of the free CH_3. At 3-fold fcc site, CH_3 interacts with three Co atoms at the fcc site, and at 3-fold hcp site, CH_3 interacts with three Co atoms on the surface by occupying hcp site for which the carbon is bound to Co atoms with the formation of three Co-C bonds. Initial structure at the bridge site is also optimized into that at the hcp site (Huang *et al.,* 2010).

The stable adsorption of CH_3 on Co(111) was proved by the change of LDOS profiles of bare and coordinated C of CH_3 atom; the change in the LDOS profile upon adsorption is given for CH_3 molecule in its free and hcp-coordinated forms (Figure 4.5). The positions of the CH_3 molecular orbitals are also indicated, and it is clear how these orbitals have moved upon adsorption. The lowest energy peak corresponds to the 2a1 derived orbital at -14.0 eV, next in energy are the 1e derived states at -7.5, and the broad peak between −7.0 and −5.0 eV corresponds to 3a1 derived states (Michaelides *et al.,* 1999). According to these LDOS profiles, the main contribution to the bonding between methyl and the metal comes from the interaction between 3a1 orbital and Co-d orbitals. Figure 4.5 shows that there is a decrease in electron density around carbon in the corresponding energy levels after chemisorptions meaning that C of CH_3 shows a electronic property similar to d bands of metals. Additionally, it was seen that the

coordinated electron density of C of CH_3 significantly shifted downward compared to that of C of free CH_3.

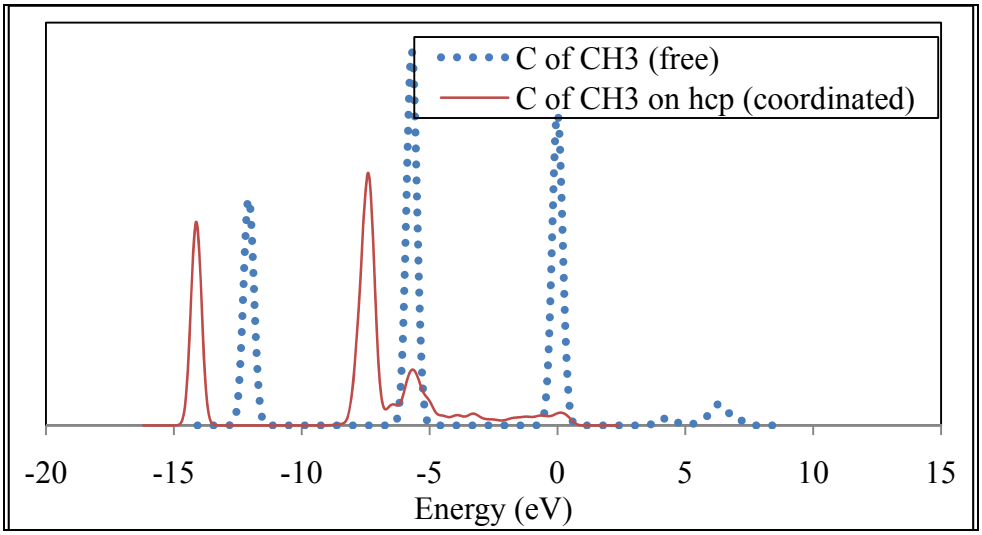

Figure 4.5. Changes in LDOS C of adsorbed CH_3 molecule on H_{hcp} at 0.25 ML.

4.5. CO Adsorption on Co(111)

The strengths of CO adsorptions on the possible sites at a constant surface coverage of 0.25 ML were analyzed. In order to simulate this surface coverage, one CO molecule was placed on a (2×2) unit cell (Figure 4.1). CO adsorption energies on these four sites, i.e. top (T), bridge (B), hollow hcp (H_{hcp}) and hollow fcc (H_{fcc}) are reported in Table 4.4.

Table 4.4. Energy of CO adsorption on Co(111). The values correspond to total adsorption energy per unit cell. The distance of C from the nearest Co atom is exhibited as d(Co-C).

Site	E_{ads} (CO) (eV)	$d_{C\text{-}Co}$ (Å)
T	-1.9926	1.7380
H_{fcc}	-2.1565	1.9760
B	-2.0434	1.9000
H_{hcp}	-2.1534	1.9650

The lowest CO adsorption energy indicating strongest adsorption was obtained on the H_{fcc} site; this was almost same with the adsorption energy of CO on the H_{hcp} site. The

maximum difference between the adsorption energies for the sites considered is very small, i.e. 0.08 eV, indicating a flat potential energy surface for CO adsorption. In terms of bond length between CO and nearest Co atom, the strongest adsorption site was atop. As the bond lengths between CO and nearest Co atom on H_{hcp} and H_{fcc} sites are longer than other sites, their adsorption strengths are slightly lower than others. Similar results were obtained by Pick*et al.* with DFT calculations; Pick concluded that proposed correction to adsorption energy of CO on Co(111) preferred the atop site, whereas the remaining sites were almost degenerate in energy (Pick*et al.,* 2007; Abild-Pedersen *et al.,* 2007). In this study, the reason of the high CO adsorption energy calculated for adsorption on atop site results from the neglected relativistic effects in calculations. On the other hand, as the values are close enough for the current work, no correction factor was used to correct the adsorption preference.

The comparison of the LDOS profiles of bare and atop CO-coordinated Co atom showed a significant shift in electron density, which indicated extensive CO-Co, interaction electronic and strong adsorption (Figure 4.6-a). Figure 4.6-b shows the change in the LDOS of H_{hcp} CO-coordinated Co atom compared to that of its bare state. Rather limited electron density shift for the coordinated Co of the H_{hcp}-site compared to that at atop site is due to the fact that at hcp site three Co atoms are coordinated with the CO molecule, and e^- density shift is given for only one of those in Fig. 4.6-b. Note that LDOS change of the Co atoms present in H_{fcc} and bridge sites led by adsorption are very similar to that for the Co atom in H_{hcp} site.

It was observed that the changes of LDOS profiles at the CO coordinated Co atom are almost the same for all sites as seen from Figure 4.6-c. LDOS profiles of carbon end of free CO were also given in Figure 4.6-c as a reference for comparison. In a CO-metal system the 3σ, 4σ, 1π, 5σ and 2π molecular orbitals of CO are essential to describe the bonding of molecule; and these molecular orbitals should be investigated in three groups: (1) The 3σ orbital hardly interacts with the metal bands due to its low energy level, and is essentially not involved in chemisorption. (2) The 4σ and 1π orbitals do interact, particularly with the metal d bands, but all the levels so formed lie below the Fermi level and the net contribution to the chemisorption energy is rather small. (3) The 5σ and 2π orbitals are, however, mixed sufficiently strong to produce unfilled antibonding states

above the Fermi level; which therefore provide significant net bonding to the surface. Consequently, 4σ-, 1π- and 5σ-derived levels contain metal orbital character; and metal-derived levels themselves contain strong 5σ, 2π and some 4σ, 1π character. The main metal-5σ and metal-2π antibonding states are located above the Fermi level (Sümer *et al.,* 2006).

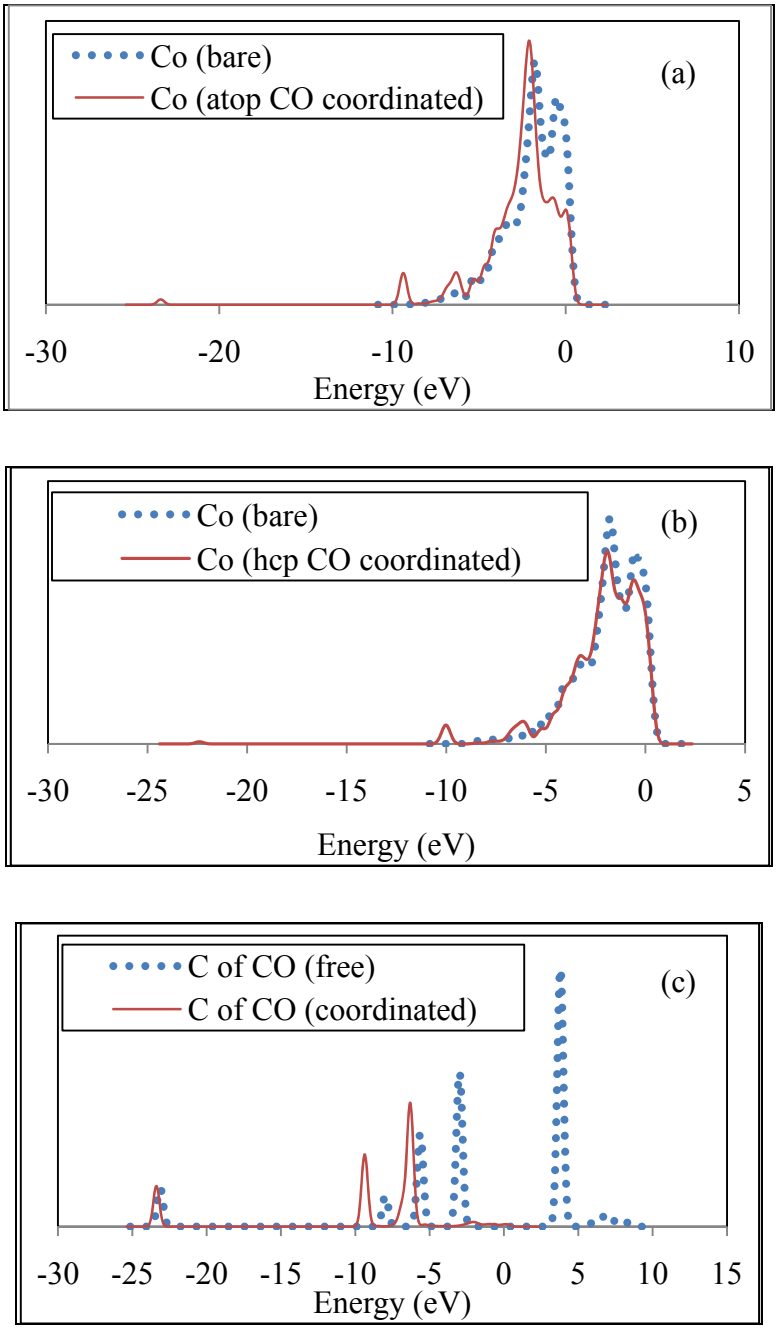

Figure 4.6. Changes in LDOS (a) atop CO-coordinated Co atom (b) H_{hcp} CO-coordinated Co atom (c) C of adsorbed CO molecule at 0.25 ML.

There are three distinct electron-rich regions along the energy scale for carbon end of coordinated-CO: the first peak at -23 eV corresponds to the 3σ state and the second peak around -9.5 eV is the 4σ state. The next peaks at -6 eV belong to the 1π state. In Figure 4.6-c, LDOS profiles of bare CO and coordinated CO are significantly different at 4σ and 1π states, proving the electronic interaction between CO molecule and the Co surface. The peaks represent the 4σ- and 1π derived states, which is at -8 eV, -5.5 eV respectively for C of free CO, is shifted downward with different amplitude for CO-Co case. The next peak in Figure 4.6-c represent the 5σ-like derived states for C of free CO. The most significant contribution comes from the 5σ molecular orbital, as the peak was vanished with respect to the corresponding peak of CO orbital, which clearly indicates that there is a decrease in electron density around carbon in the corresponding energy levels after chemisorption.

These important changes in all LDOS profiles and high adsorption energies of CO prove that CO adsorption is stable on the Co surface. This confirms that CO as a product of CDRM stable and can be formed on Co active centers of the catalyst at the end of the reaction.

4.6. O Adsorption on Co(111)

The strengths of O adsorptions on the possible sites at a constant surface coverage of 0.25 ML were analyzed. In order to simulate this surface coverage, one O atom was placed on a (2×2) unit cell (Figure 4.1). O adsorption energies on these four sites, i.e. top (T), bridge (B), hollow hcp (H_{hcp}) and hollow fcc (H_{fcc}) are reported in Table 4.5.

The O adsorption energies in Table 4.5 were almost the same stemming from the fact that O molecule positioned at atop, H_{fcc} and bridge type coordination position assumes H_{hcp} type coordination at the end of the energy/geometry optimization. The results show that oxygen adsorption is only stable on H_{hcp} site of Co(111), with an adsorption energy of -7.6468 eV. This result was proved by obtaining the same bond lengths between O and nearest Co atom, 1.8380 Å for all sites (Figure 4.7). Additionally, results confirm that oxygen interacts with all possible Co adsorption sites other than H_{hcp} will diffuse to H_{hcp} site.

Table 4.5. Energy of O adsorption on Co(111). The values correspond to total adsorption energy per unit cell. The distance of O from the nearest Co atom is exhibited as d(Co-O).

Site	E_{ads}(O) (eV)	$d_{C\text{-}Co}$ (Å)
T	-7.6464	1.8380
H_{fcc}	-7.6468	1.8380
B	-7.6462	1.8380
H_{hcp}	-7.6464	1.8380

The LDOS profiles differences of bare and coordinated oxygen atoms on Co explain the stable oxygen adsorption on H_{hcp} site (Figure 4.8).

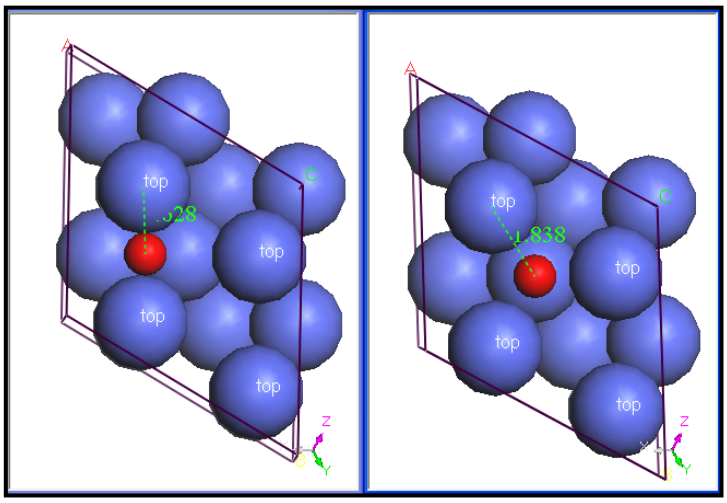

Figure 4.7. Initial and final structures of O adsorption on bridge site at 0.25 ML.

There are two distinct electron-rich regions along the energy scale for coordinated-O: the first peak at -19.5 eV corresponds to the 2s state and the second peak around -6.0 eV is the 2p state. In Figure 4.8, LDOS profiles of free and coordinated O are significantly different at 2p states, proving the electronic interaction between O molecule and Co surface. The peaks represent the 2p derived state, which is at -5.0 eV for free O, is shifted downward with different amplitude for O-Co case. The most significant contribution comes from the 2p molecular orbital, as the peak got smaller with respect to the corresponding peak present at free O; which clearly indicates that there is a decrease in electron density around oxygen in the corresponding energy levels after chemisorptions.

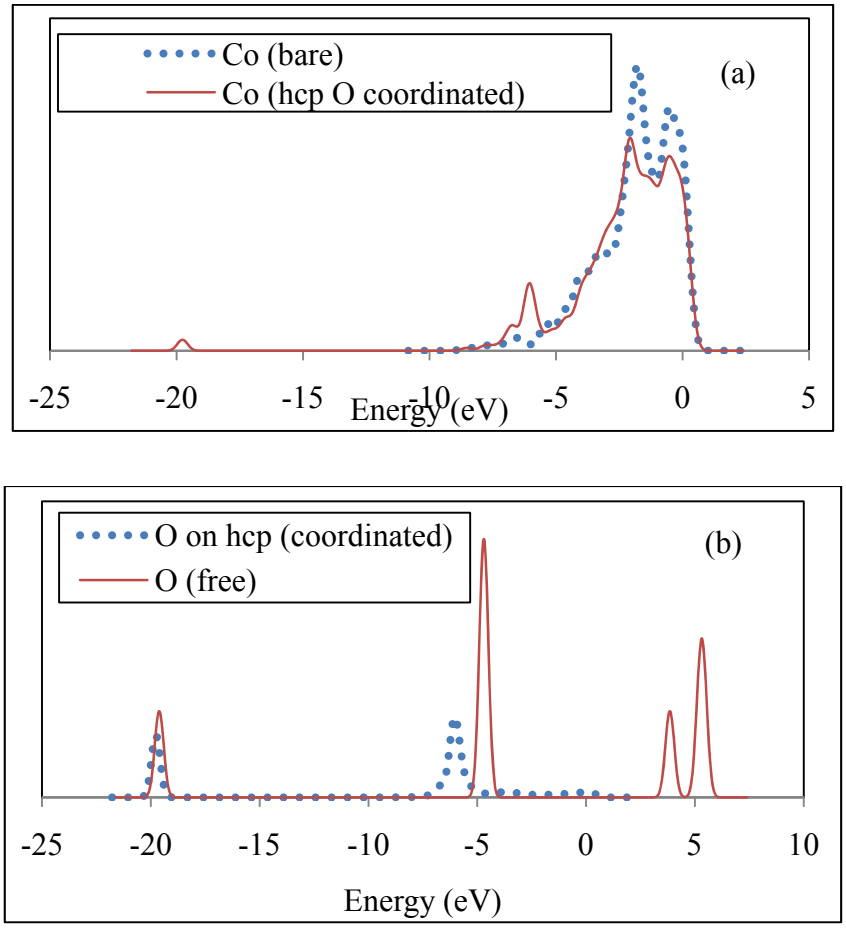

Figure 4.8. Changes in LDOS (a) H_{hcp} O-coordinated Co atom (b) O molecule at 0.25 ML.

4.7. Methane Dehydrogenation

Aiming to understand the way methane activation and dehydrogenation process occurs on Co(111) surface, all the elementary steps of the dehydrogenation starting from CH_4 to surface C were studied with transition stage (TS) searches.

Activation energy barriers for each of the below elementary steps on the Co(111) surface was calculated:

$$CH_4^* \rightarrow CH_3^* + H^* \rightarrow CH_2^* + 2H^* \rightarrow CH^* + 3H^* \rightarrow C^* + 4H^* \qquad (4.2)$$

Prior to each transition search study, CH_4, CH_3, CH_2 and CH species were initially positioned at H_{hcp} site. The optimized transition state energy profiles obtained via

structures using the complete LST/QST method are shown in Figure 4.9. The energy barriers of the most favored elementary steps for forward and backward direction as well as the corresponding reaction energy values computed in this study are listed in Table 4.6.

As shown in Table 4.6, CH_4 dissociation into CH_3+H needs to overcome a barrier of 0.1 Ha while the energy barrier for the backward reaction is 0.046 Ha. The energy barrier of CH_3 dehydrogenation into CH_2+H is 0.065 Ha, and that of its back reaction is 0.032 Ha. The results show that CH_3 dehydrogenation into CH_2 and H is easier compared to CH_4 dissociative adsorption. Dehydrogenation of CH_2 to CH needs to overcome the energy barriers of 0.06 Ha which is rather lower than those of CH_4 and CH_3 dehydrogenation. Lowest activation energy was obtained for CH_2 dehydrogenation. Further dehydrogenation, CH to C+H needs to overcome a barrier of 0.072 Ha, and its back reaction barrier is 0.015 Ha. Besides, CH dissociation into C+H has the highest endothermicity among in four steps.

Table 4.6. Energetics of the most favored elementary steps in CH_4 dehydrogenation on Co(111).

		Forward Reaction Barrier (Activation Energy) (Ha)	**Back Reaction Barrier (Ha)**	**ΔE (Ha)**
CH_4*↔CH_3*+H*	**TS1**	0.1	0.046	0.054
CH_3*↔CH_2*+H	**TS2**	0.065	0.032	0.033
CH_2*↔CH*+H	**TS3**	0.06	0.013	0.047
CH*↔C*+H*	**TS4**	0.072	0.015	0.057

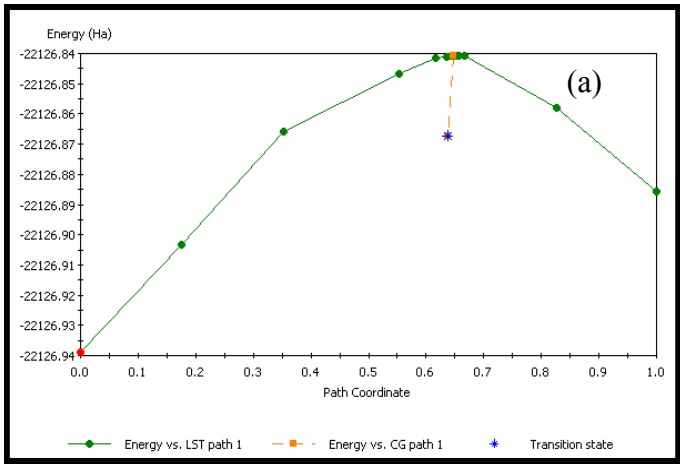

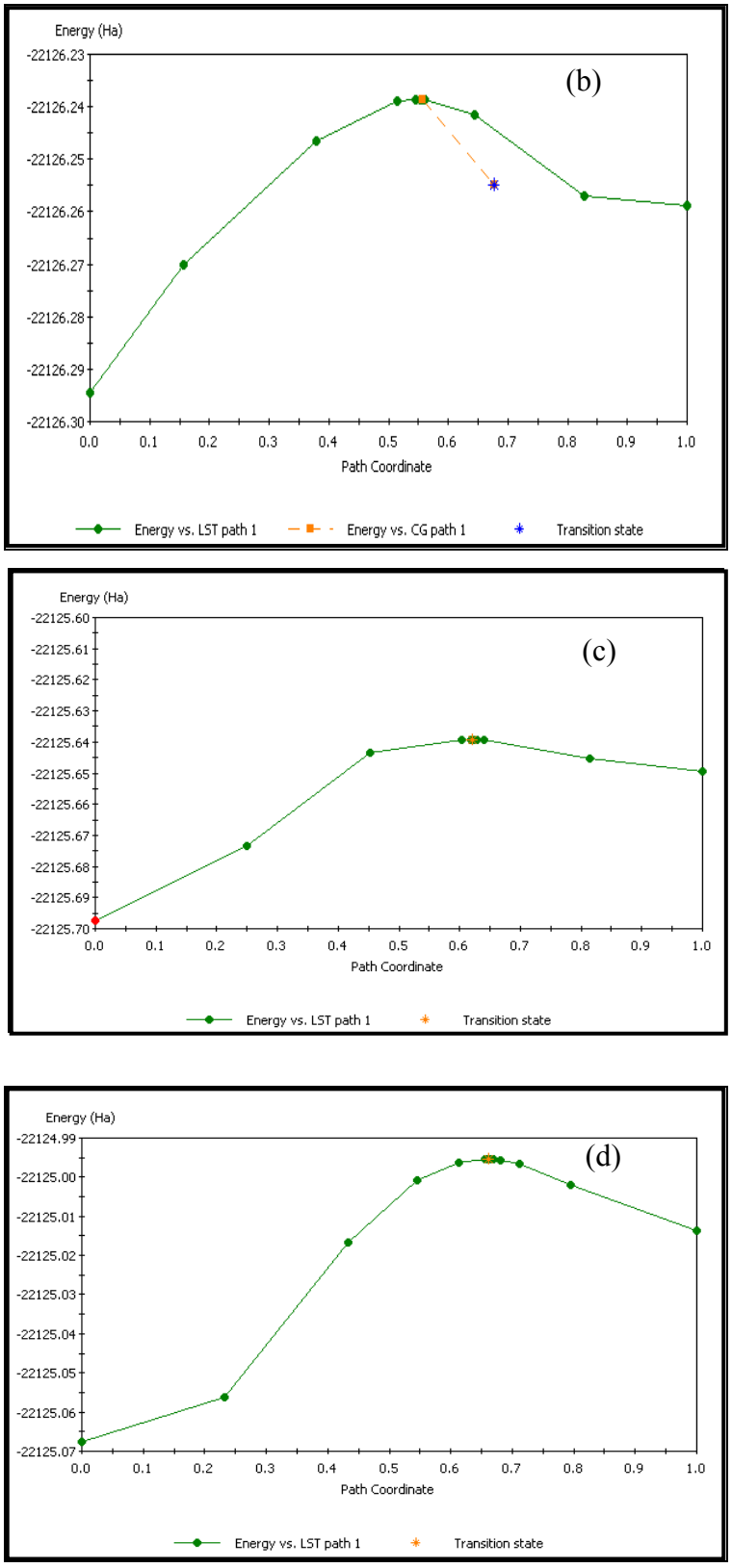

Figure 4.9. TS searches and the energy barriers (Ha) of (a) CH_4dehydrogenation as $CH_4 \leftrightarrow CH_3+H$ (b) CH_3dehydrogenation as $CH_3 \leftrightarrow CH_2+H$ (c) CH_2dehydrogenation as $CH_2 \leftrightarrow CH+H$ (d) CH dehydrogenation as $CH \leftrightarrow C+H$.

4.8. Effect of Surface Coverage on Coadsorption of C+O

In order to investigate the effect of surface concentration on the adsorption energy and geometry of C and O coadsorption system, three coadsorption combinations in terms of surface concentration were studied; there the surface concentrations used were 0.25 ML C and 0.25 ML O making the total surface coverage 0.5 ML; 0.5 ML C and 0.25 ML O making the total surface coverage 0.75 ML; finally 0.25 ML C and 0.5 ML O making surface coverage 0.75 ML. For coadsorption systems, the system allowing site competition means that there is surface metal(s) atom in the system which has/have bonds with both adsorbates.

Table 4.7.Adsorption types and system total energies C+O coadsorptions on Co(111).

Surface Concentration (ML)		**Adsorption type**		**System Total Energy (eV)**
C	**O**	**C**	**O**	
0.25	0.25	H_{hcp}	H_{fcc}	-17271.7173
0.25	0.25	Atop	atop	-17271.7925
0.25	0.50	Atop	atop & H_{hcp}	-17708.7965
0.25	0.50	atop & atop	atop	-17707.4773
0.50	0.25	atop & atop	H_{hcp}	-17425.7574
0.50	0.25	atop & atop	atop	-17425.8683

It should be noted that in order to see both the changes in the extent of interaction between the adsorbates and the final configurations in response to whether there is a site competition, different adsorption site combinations for C and O were used for each of the surface concentration combination. It should be noted that in coadsorption the interactions between the adsorbates are not limited to direct, adsorbate-adsorbate type, interactions but also include the indirect, surface-mediated type.

At the total surface coverage 0.5 ML, the tendency of CO formation was investigated by using different initial coadsorption configurations. Figure 4.10 shows that starting with the initial coadsorption system allowing site competition for which O positioned at H_{fcc} site, and C positioned at H_{hcp} site, a stable final structure which is the adsorbed CO

molecule at the H_{hcp} site of Co(111) was obtained at the end of energy optimization. However, it was seen that if there is no site competition between C and O atoms as in the coadsorption system for which both O and C were positioned at atop sites, there was no CO formation (Figure 4.11) in spite of the CO formation tendency observed as in the case of site competition.

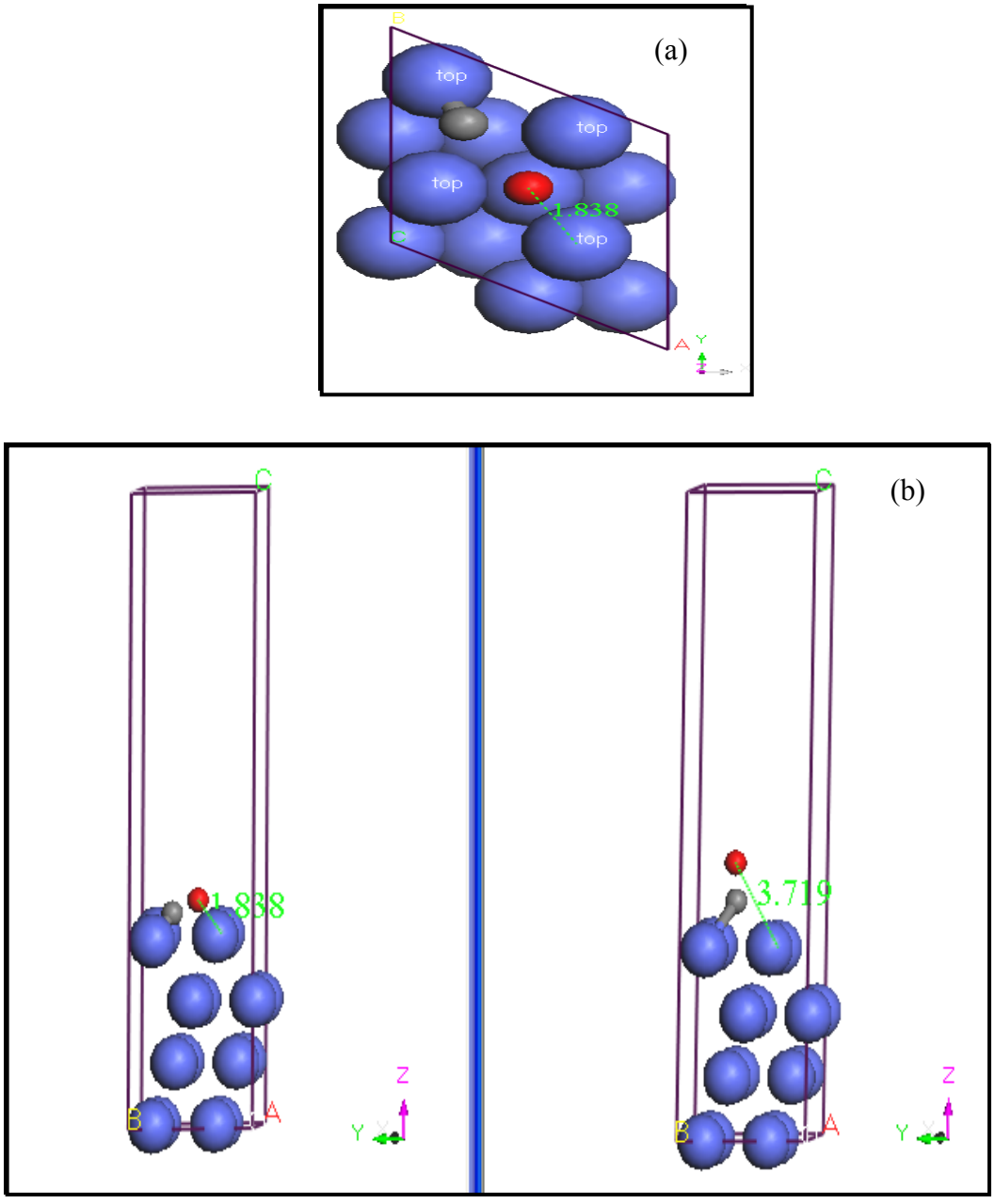

Figure 4.10. (a) The top view of initial structure of the coadsorption of O at H_{fcc} site and C at H_{hcp} site (b) The change of the initial structure of coadsorption of O positioned and C to the final structure.

In order to observe the behavior of those coadsorption systems; first one oxygen atom and one carbon atom were placed on the atop sites, which gives 0.25 ML C and 0.25 ML O surface coverage making the total coverage 0.50 ML; then another oxygen atom was placed on H_{fcc} site, making surface O concentration 0.5 ML for the initial structure as given in 4.12-a; for this system the CO molecule was formed on the atop site in the energy optimized final state and the other oxygen atom was adsorbed and stabilized on H_{hcp} site (Figure 12-c), which was found as the most stable site for oxygen adsorption previously.

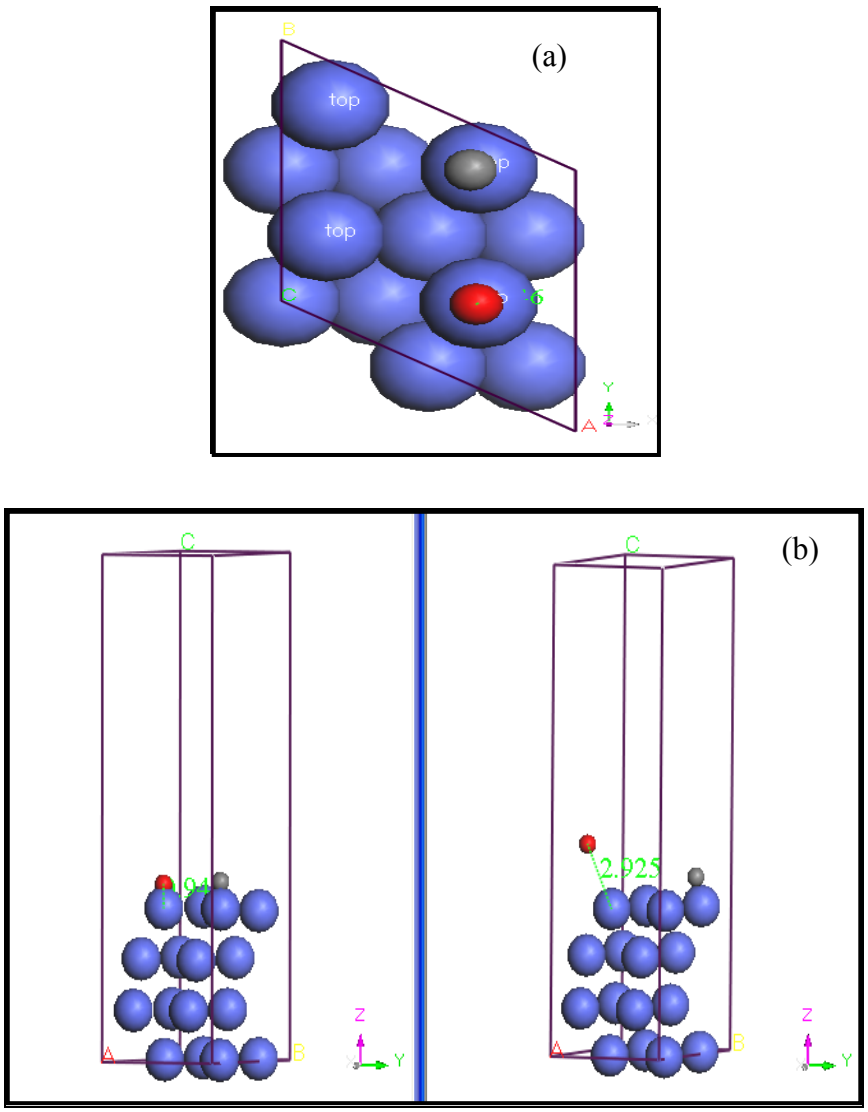

Figure 4.11. (a) The top view of initial structure of the coadsorption of O at atop site and C at atop site (b) The change of the initial structure of coadsorption of O and C to the final structure.

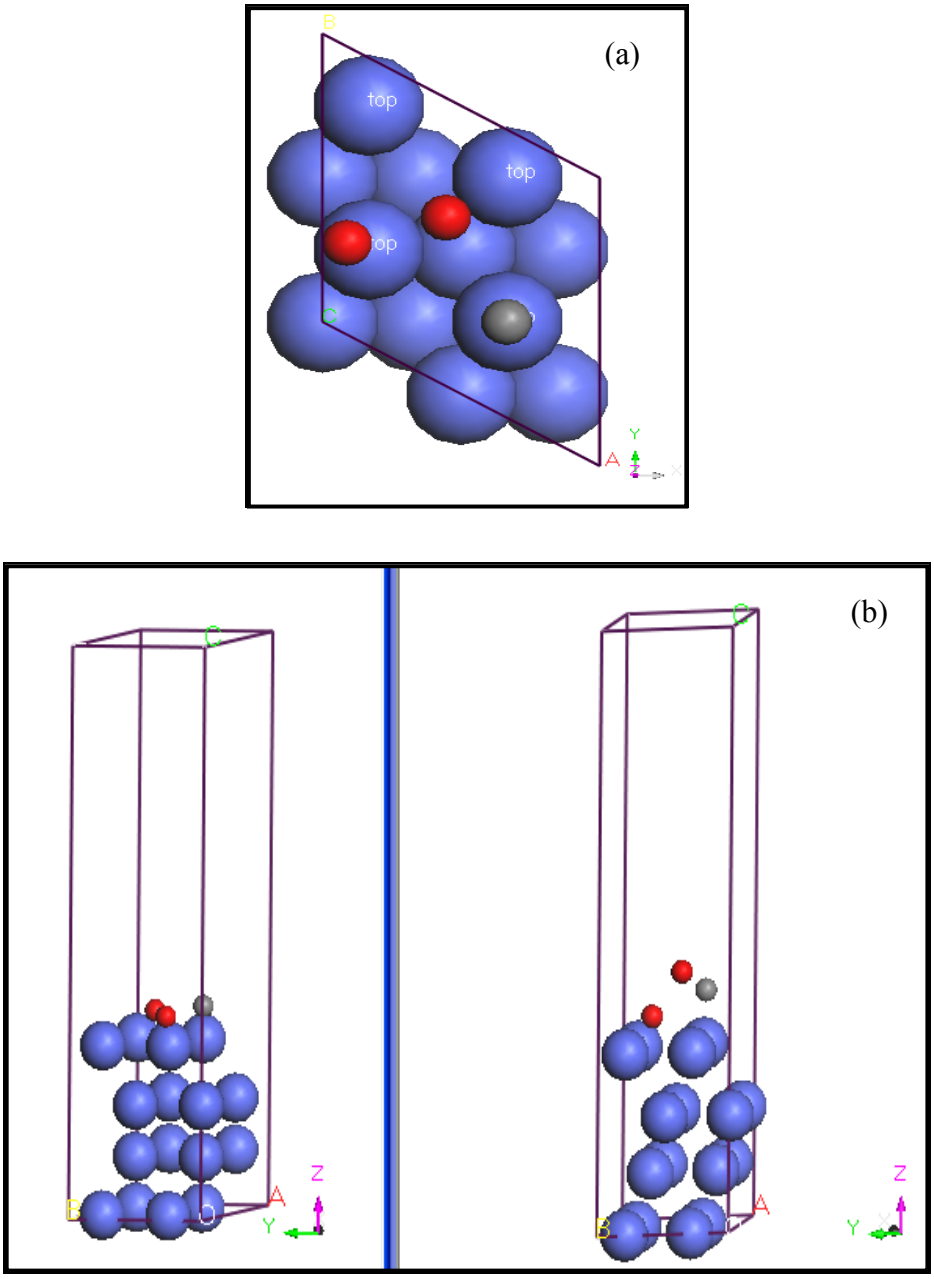

Figure 4.12. (a) The top view of initial structure of the coadsorption of 2O at atop and H_{hcp} sites and C at atop site (b) The change of the initial structure of coadsorption of 2O and C to the final structure.

As the second coadsorption system, both oxygen atoms and carbon atom were placed on atop sites initially making surface oxygen and concentrations 0.5 ML and 0.25 ML, respectively, at the starting point. For that system, there is no site competition between the adsorbents. However, though as a final structure, all atoms moved to their stable sites with the tendency of CO formation, CO molecule could not form (Figure 4.13-b&c) most

probably due to the lack of site competition, which is parallel to the result obtained for 0.5 ML total surface coverage with equal O and C surface concentrations allowing no site competition.

At the total surface coverage 0.75 ML carbon rich surface, i.e. Co(111) surface having 0.5 ML carbon, 0.25 ML oxygen was also studied for adsorption configurations with and without site competition and the tendency for CO formation was investigated. In both cases, C atoms was placed on the surface at atop sites the surface at giving 0.5 ML surface carbon concentration, whereas for O atom was placed at different sites; at H_{hcp} site (Figure 4.14) and at atop site (Figure 4.15).

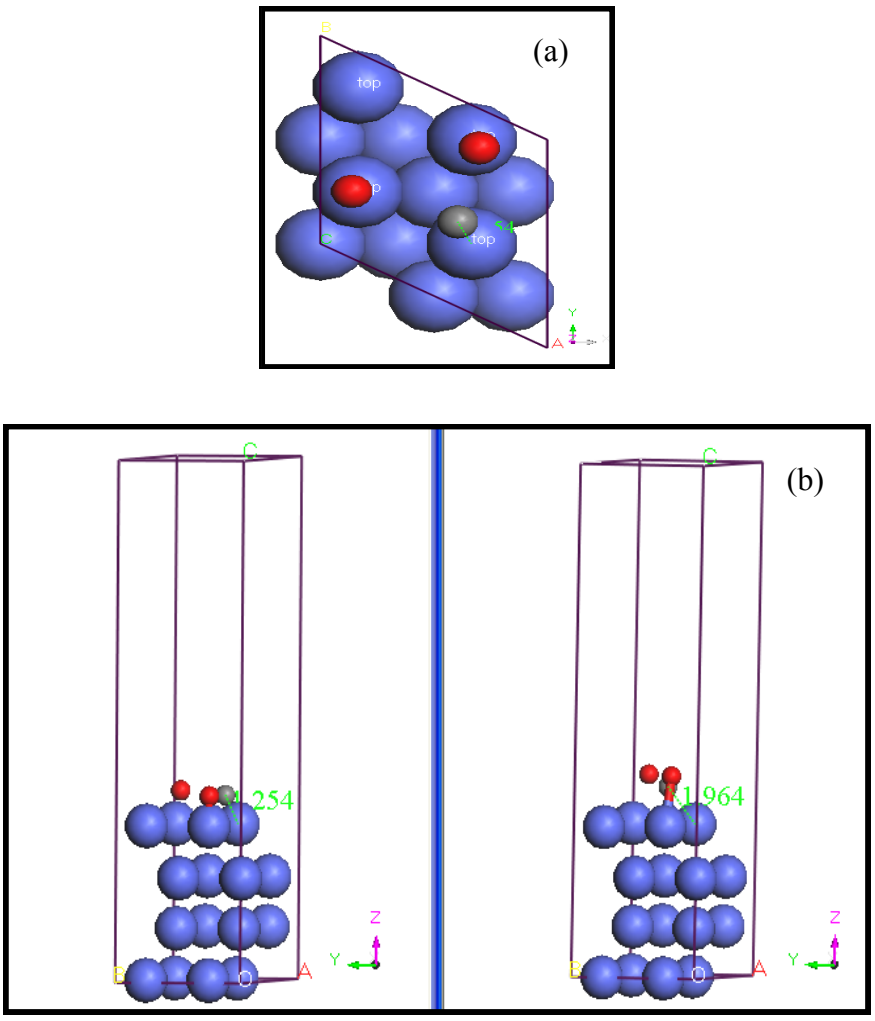

Figure 4.13. (a) The top view of initial structure of the coadsorption of 2O at atop sites and C at atop site (b) The change of the initial structure of coadsorption of 2O and C to the final structure.

In the energy optimized structure of the former case CO molecule was formed on atop site which has a C atom initially and the other carbon atom was stable on H_{hcp} site (Figure 4.14). In the latter case for which all oxygen and carbon atoms were placed on the atop sites as the initial coadsorption configuration preventing site competition, the oxygen and one of the carbon atoms left the surface as CO molecule while the other carbon atom assumes bridge position on the surface upon the energy optimization (Figure 4.15).

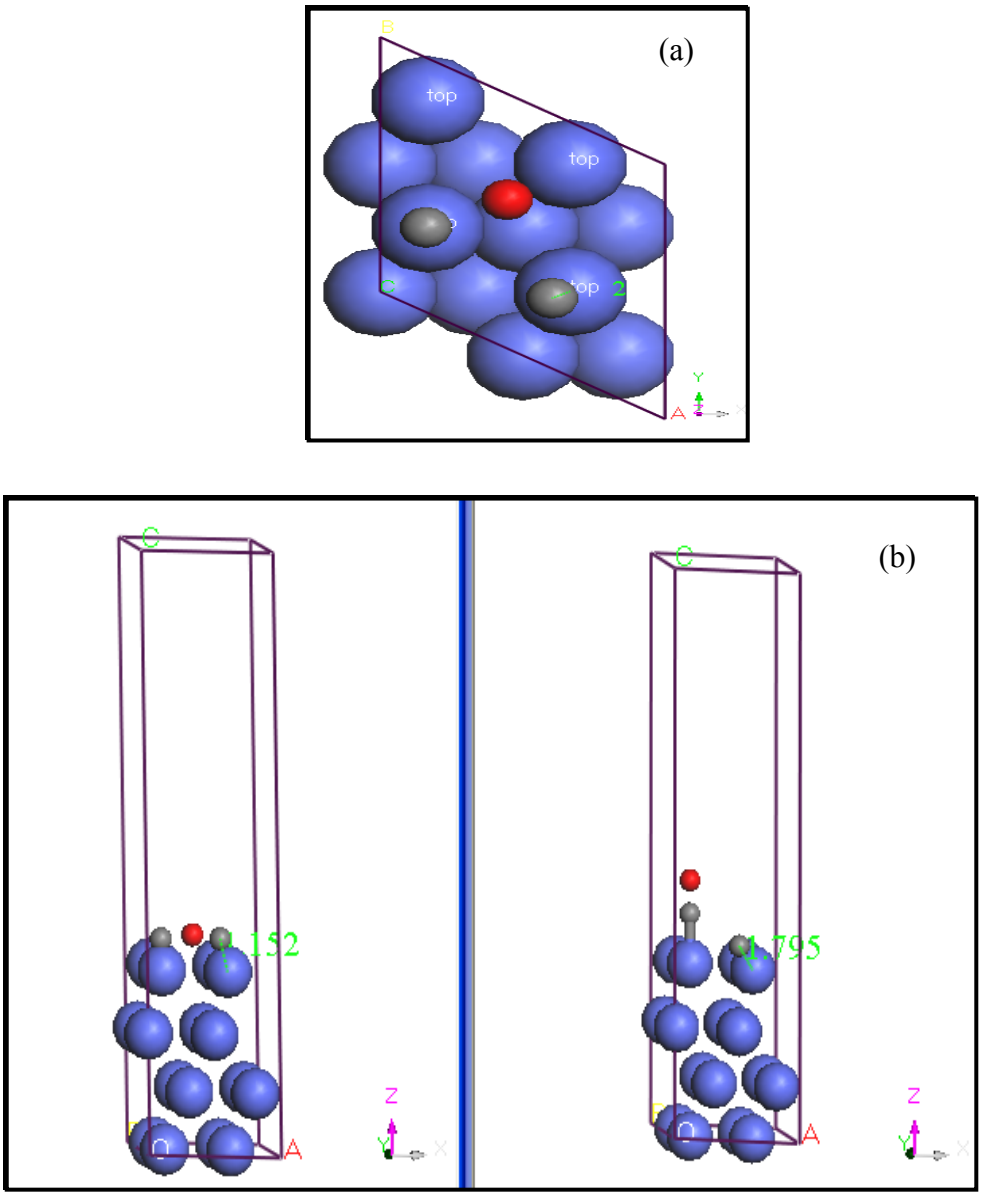

Figure 4.14. (a) The top view of initial structure of the coadsorption of O at H_{hcp} site and 2C at atop sites (b) The change of the initial structure of coadsorption of O and 2C to the final structure.

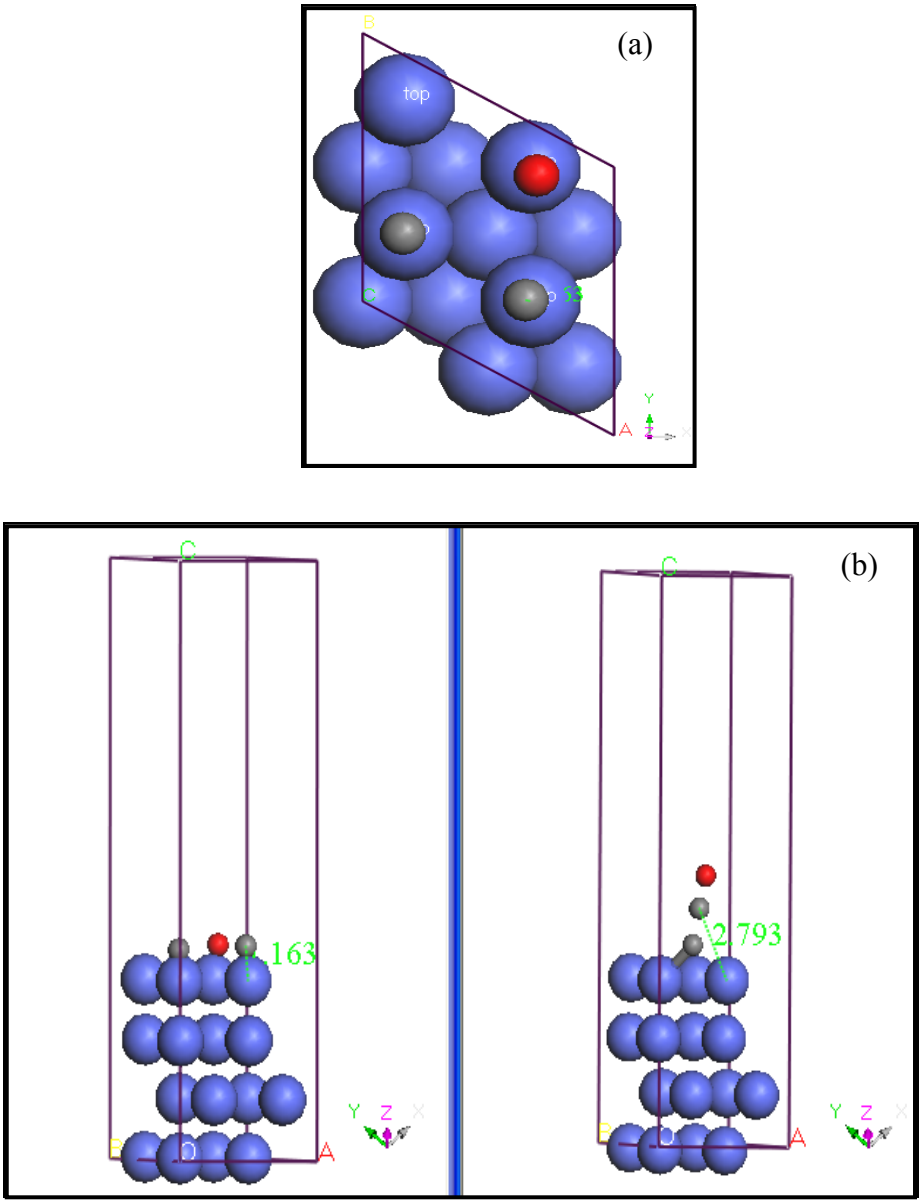

Figure 4.15. (a) The top view of initial structure of the coadsorption of O at atop site and 2C at atop sites (b) The change of the initial structure of coadsorption of O and 2C to the final structure.

4.9. CO and CH_3 Coadsorption

CO and CH_3 surface coverages are both taken as 0.25 ML for the CO+CH_3 coadsorption system making total surface coverage 0.5 ML. Two different CO and CH_3 adsorption site combinations were studied considering stability/adsorption strength of individual CO and CH_3 on the sites of Co(111). Those coadsorption systems studied are

$CO\text{-}H_{hcp}$ + $CH_3\text{-}H_{hcp}$, and $CO\text{-}H_{fcc}/H_{hcp}$ + CH_3-bridge configurations. The initial coadsorption configuration of the systems are given in Figures 4.16-a&b, and 4.17-a&b, and the configuration of the systems upon energy optimization are given in Figures 4.16-c and 4.17-c, respectively.

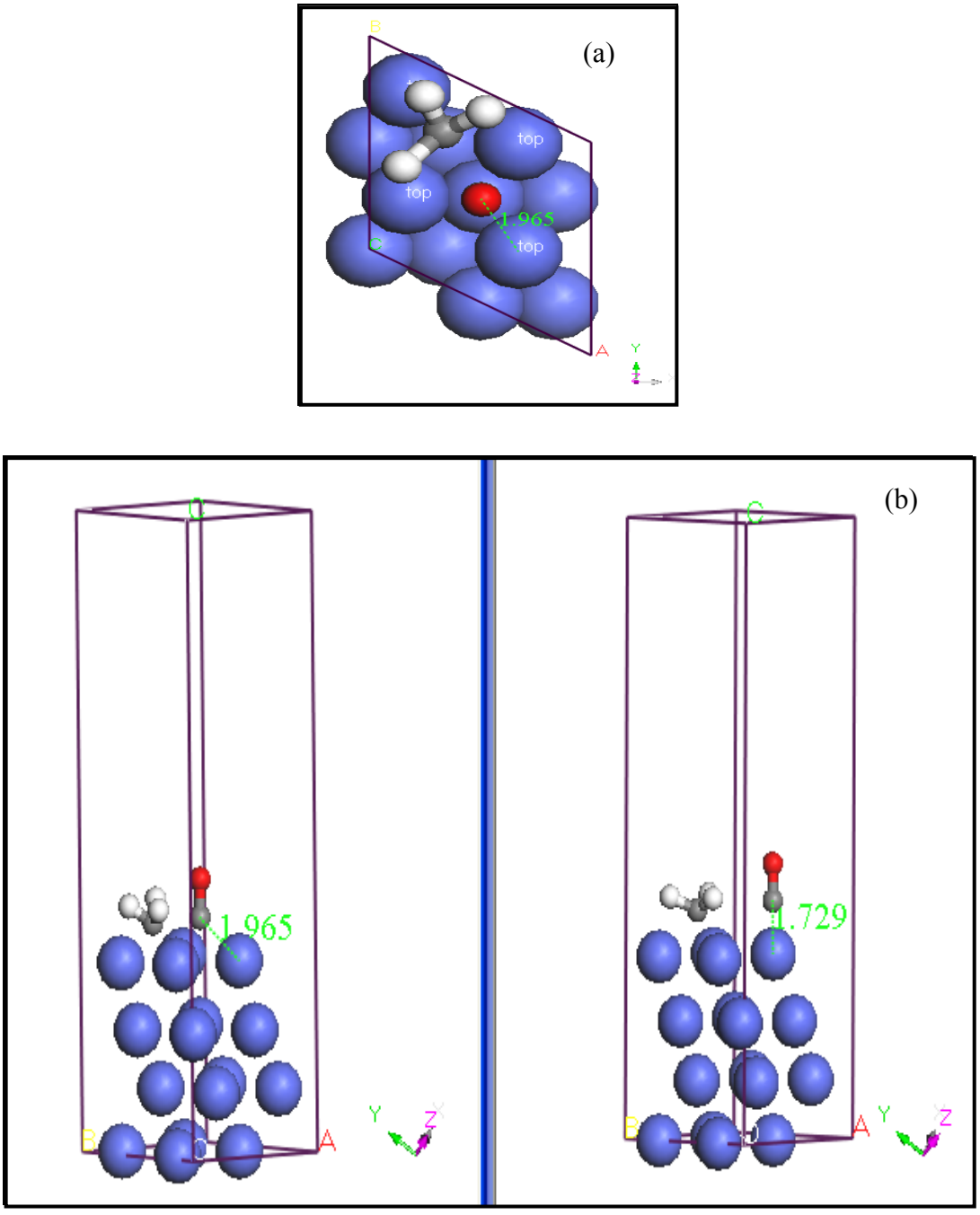

Figure 4.16. (a) The top view of initial structure of the coadsorption of CO at H_{hcp} site and CH_3 at H_{hcp} site (b) The change of the initial structure of coadsorption of CO and CH_3 to the final structure.

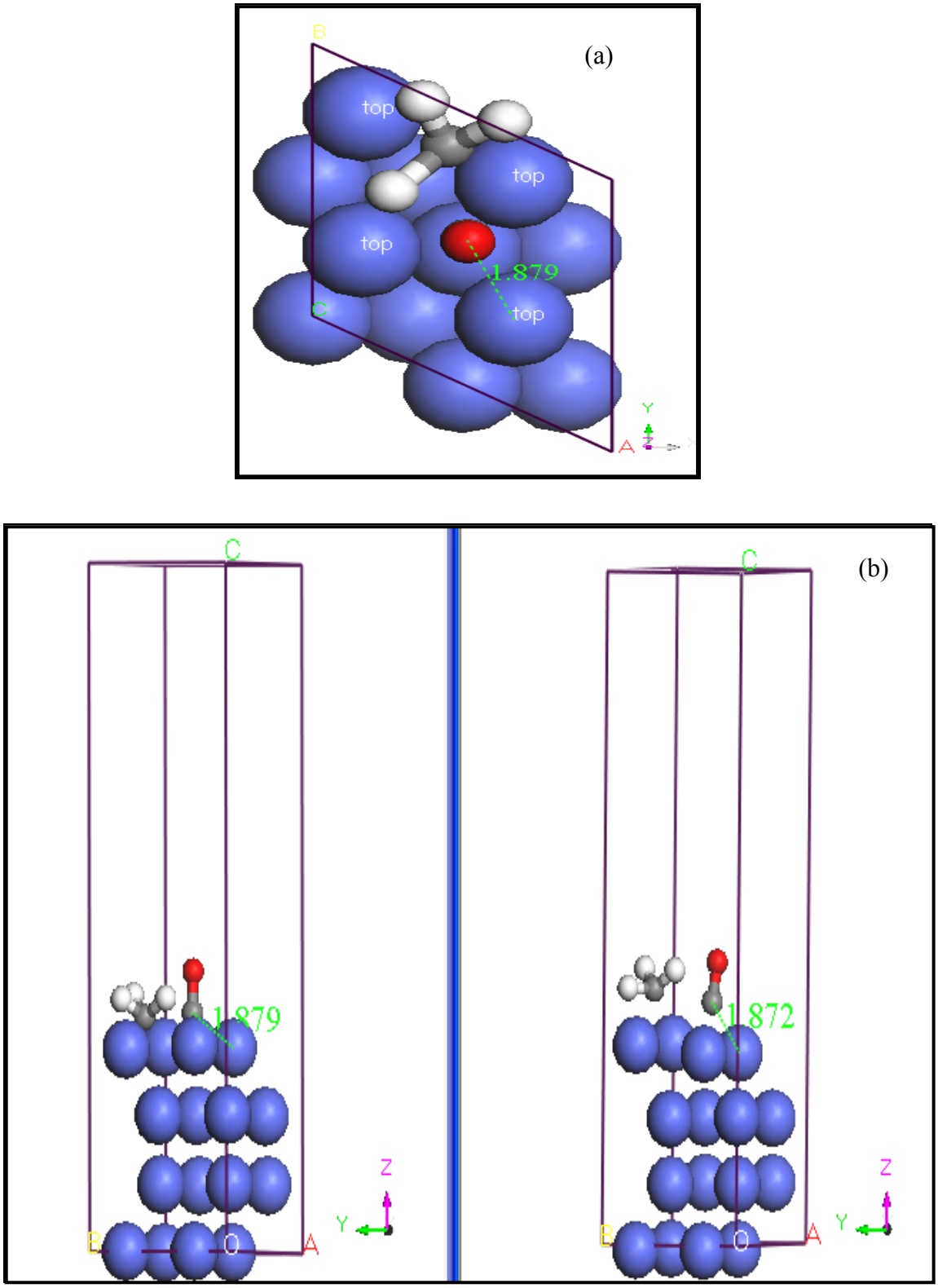

Figure 4.17. (a) The top view of initial structure of the coadsorption of CO at H_{fcc}-H_{hcp} sites and CH_3 at bridge site (b) The change of the initial structure of coadsorption of CO and CH_3 to the final structure.

The total coadsorption energy change for each system is given in the Table 4.8, which was calculated by using Equation 4.4,

$$E_{coads} = E_{ads}^{CO+CH_3} + E_{CO}^{free} + E_{CH_3}^{free} \quad (4.4)$$

It should be noted that the calculation is possible as the energies of free CO and CH_3 molecules could be found through using simulations (see parts 4.4 and 4.5).

Total coadsorption energies calculated for both coadsorption configurations are exothermic indicating the stability gained. Though atop type adsorption is less stable for CH_3 as indicated by individual CH_3 adsorption studies on Co(111) (part 4.4), for CO-H_{hcp} + CH_3-H_{hcp} system CO assumes atop position and moves slightly away from the surface as can be seen from the optimized geometry indicating direct adsorbate-adsorbate interaction and site competition. As CH_3 has greater stability on H_{hcp} site, with individual adsorption energy -2.86, compared to that of CO, -2.15 eV; the change in the position of CH_3 is not significant.

Table 4.8. Adsorption types, system total and total coadsorption energies of C+O coadsorptions on Co(111).

Surface Concentration (ML)		**Adsorption type**		**System Total Energy (eV)**	**E_{coads}(eV)**
CO	**CH_3**	**CO**	**CH_3**		
0.25	0.25	H_{hcp}	H_{hcp}	-17474.8367	-4.426
0.25	0.25	H_{fcc}-H_{hcp}	bridge	-17474.6514	-4.240

In the second coadsorption configuration, CO as positioned initially at H_{fcc}/H_{hcp} considering strength of individual CO adsorption on both H_{hcp} and H_{fcc} sites are equal as -2.15 eV, and CH_3 was positioned initially at bridge site. It is interesting to see that both CH_3 and CO move slightly away from the surface in the optimized geometry, and the position change of CH_3 was associated with position change of CH_3-coordinated Co atoms of the surface. The results of the CH_3+CO coadsorption system indicates that the direct

CH_3-CO interaction yielding a reaction intermediate/product has very limited possibility as both species are stable at the surface as indicated by energy optimized configurations.

4.10. CO Formation from C+O

It is known from our previous experimental studies and the results presented in the literature that during CDRM the surface carbon formed on metal sites is cleaned by surface oxygen produced by CO_2 dissociation on the catalyst support, which then transferred to the metallic sites. In this study, CO formation through the reaction between coadsorbed surface C and O was studied on Co(111) surface with transition stage (TS) searches (Figure 4.18). The energy profile of the elementary step:

$$C^*+O^* \leftrightarrow CO^* \qquad (4.3)$$

on Co(111) surface was obtained.

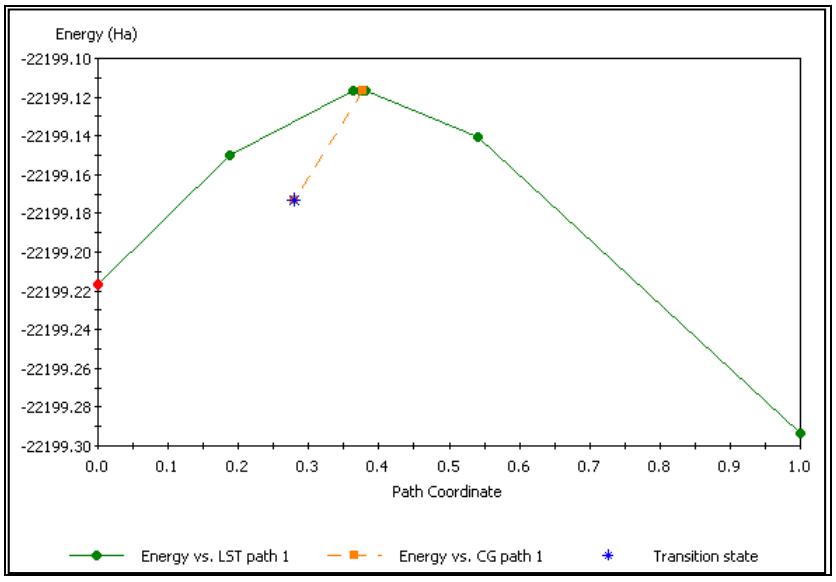

Figure 4.18. TS search and the energy barriers (Ha) of CO formation as C+O↔CO.

Prior to the TS search of CO formation on Co(111), CO molecule was initially positioned on H_{fcc} site of Co(111) for which CO adsorption has highest stability. Additionally, one of the stable C+O coadsorption structures on Co(111) was used as the final structure; in this structure it was observed that O was optimized on H_{hcp} and C was

optimized on the other H_{hcp} site of Co(111) unit cell. The optimized transition state energy profile obtained via using the complete LST/QST method is shown in Figure 4.18.

The calculated energy barriers for the forward (C + O → CO) and backward (CO → C + O) directions are 0.1 Ha and 0.18 Ha, respectively, yielding an exothermic reaction with reaction energy, ΔE; as -0.08 Ha. The exothermicity indicates that CO formation on Co(111) surface is favorable both kinetically and thermodynamically.

5. CONCLUSIONS AND RECOMMENDATIONS

5.1. Conclusions

CO_2 was adsorbed on all sites of Co(111) surface but adsorption energies and LDOS profiles shows that the strengths CO_2 adsorption on those sites are very low. On the other hand, CH_4 adsorption is either unstable or yields CH_3 and H stabilized on the surface.

CO adsorptions on all Co(111) sites were found very strong with very similar adsorption energies. CH_3 adsorption is stable on all Co(111) sites, except on the bridge site, and the adsorption is strong. CH_3 initially placed at bridge position assumed hcp position upon energy optimization. The most favorable sites for CH_3 and CO adsorptions were H_{hcp} and atop sites, respectively.

Simulation results show that oxygen adsorption is stable only at H_{hcp} site of Co(111) as O adsorbed on other sites assume H_{hcp} position upon energy optimization.

C and O coadsorption studies revealed that the energy optimized structures are very sensitive to relative surface coverages of the adsorbates as well as whether there is site competition between them; C and O interaction yield CO only when there is site competition for the initial coadsorption system.

The transition stage (TS) searches of CH_4 dehydrogenation steps forming hydrogen and surface carbon revealed that CH_4 dehydrogenation step is the rate-determining step of CH_4 dissociative adsorption on Co(111) surface. Since CH dehydrogenation has high energy barrier and the strong endothermicity, CH dehydrogenation was found unfavorable both kinetically and thermodynamically.

The transition stage (TS) search analysis of reaction between surface C and O showed that CO formation is an exothermic process, and is favorable on Co(111) .

5.2. Recommendations

TS searches, adsorption and coadsorption calculations for all adsorbates should be carried out for Co-Ce and Co-La surface alloy catalysts that are active catalysts for CDRM (Özkara-Aydınoğlu *et al.,* 2010).

To determine and analyze the frequencies of the dry reforming reactants (CO_2 and CH_4), products (CO and H_2) and intermediate products (CH_3, CH_2, CH and C) on Co surface further, vibrational frequency analysis should be carried out by DFT and these results should be confirmed experimentally through the use of FTIR-DRIFTS.

REFERENCES

Accelrys Inc., Materials Studio CASTEP, Accelrys Inc., San Diego, 2001.

Accelrys Inc., Materials Studio DMOL3, Accelrys Inc., San Diego, 2001.

Abild-Pedersen, F. and M. P. Andersson, 2007, "CO Adsorption Energies on Metals with Correction for High Coordination Adsorption Sites - a Density Functional Study", *Surface Science,* Vol. 601, pp. 1747.

Adesina, A. A., S. Y. Foo, C. K. Cheng and T. Nguyen, 2010, "Kinetic Study of Methane CO_2 Reforming on Co-Ni/Al_2O_3 and Ce-Co-Ni/Al_2O_3 Catalysts", *Catalysis Today,* doi:10.1016/j.cattod.2010.10.092.

Bartholomew, C. H., 2001, "Mechanisms of Catalyst Deactivation", *Applied Catalysis A: General*, Vol. 212, pp. 17-60.

Boukha, Z., M. Kacimi, M. F. R. Pereira, J. L. Faria, J. L. Figueiredo and M. Ziyad, 2007, "Methane Dry Reforming on Ni Loaded Hydroxyapatite and Fluoroapatite", *Applied Catalysis A: General*, Vol. 317, pp. 299-309.

Bradford, M. C. J. and M. A. Vannice, 1999, "CO_2 Reforming of CH_4 Catalysis Reviews: Science and Engineering", *Catalysis Reviews,* Vol. 41, pp. 1-42.

Chen, D., R. Lødeng, A. Anundskås, O. Olsvik and A. Holmen, 2001, "Deactivation during Carbon dioxide Reforming of Methane over Ni Catalyst: Microkinetic Analysis", *Chemical Engineering Science*, Vol. 56, pp. 1371-1379.

Cheng, D., X. Zhu, Y. Ben, F. He, L. Cui and C. Liu, 2006, "Carbon Dioxide Reforming of Methane over Ni/Al_2O_3 Treated with Glow Discharge Plasma", *Catalysis Today*, Vol. 115, pp. 205-210.

Chu, W., N. Wang, L. Huang and T. Zhang, 2010, "Effects of Ce/Zr ratio on the Structure and Performances of Co-$Ce_{1-x}Zr_xO_2$ Catalysts for Carbon dioxide Reforming of Methane", *Journal of Natural Gas Chemistry*, Vol. 19, pp. 117-122.

Stevens, Jr., R. W. and S. S. C. Chuang, 2004, "In Situ IR Study of Transient CO_2 Reforming of CH_4 over Rh/Al_2O_3", *The Journal of Physical Chemistry*, Vol. 108, pp. 696-703.

Clark S. J., M. D. Segall, C. J. Pickard, P. J. Hasnip, M. J. Probert, K. Refson and M. C. Payne, 2005, "First Principles Methods using CASTEP", *Z. Kristallogr*, Vol. 220, pp. 567.

Dadyburjor, D. B., H. Shao, E. L. Kugler, S. A. Rykov and J. G. Chen, 2009, "Correlating NEXAFS Characterization of Co-W and Ni-W Bimetallic Carbide Catalysts with Reactivity for Dry Reforming of Methane", *Applied Catalysis A: General*, Vol. 356, pp. 18-22.

Delly, B., 1990, "An All-electron Numerical Method for Solving the Local Density Functional for Polyatomic Molecules", *Journal of Chemical Physics,* Vol. 92, pp. 508.

Delly, B., 2000, "From Molecules to Solids with the $DMol^3$ Approach", *Journal of Chemical Physics*, Vol. 113, pp. 7756.

Dinego, D. P. and M.G. Bawendi, 1999, "A Solution-phase Chemical Approach to a New Crystal Structure of Cobalt", *Angewandte Chemie International Edition,* Vol. 38, pp. 1788-1791.

Erdohelyi, A., J. Cserenyi and F. Solymosi, 1993, "Activation of CH_4 and Its Reaction with CO_2 over Supported Rh Catalysts", *Journal of Catalysis*, Vol. 141, pp 287-299.

Forzatti, P. and L. Lietti, 1999, "Catalyst Deactivation", *Catalyst Today*, Vol. 52, pp. 165-181.

Hehre, W. J., *"A Guide to Molecular Mechanics and Quantum Chemical Calculations*", Wave Function, Inc. 2003.

Hohenberg, P. and W. Kohn, 1964, "Inhomogeneous Electron Gas", *Physical Review*, Vol. 136, pp. B864.

Huang, W., Z. Zuoa, P. Hanb and Z. Li, 2010, "A Density Functional Theory Study of CH_4 Dehydrogenation on Co(111)", *Applied Surface Science*, Vol. 256, pp. 5929-5934.

Huang, W. and J. Cheng, 2010, "Effect of Cobalt (nickel) Content on the Catalytic Performance of Molybdenum Carbides in Dry-methane Reforming", *Fuel Processing Technology,* Vol. 91, pp.185-193.

Gallego, G. S., C. Batiot-Dupeyrat, J. Barrault, E. Florez and F. Mondragón, 2008a, "Dry Reforming of Methane Over $LaNi_{1-y}ByO_{3+\delta}$ (B = Mg, Co) Perovskites Used as Catalyst Precursor", *Applied Catalysis A: General,* Vol. 334, pp. 251-258.

Gallego, G. S., F. Mondragón, J. Tatibouet , J. Barrault and C. Batiot-Dupeyrat, 2008b, "Carbon Dioxide Reforming of Methane over La_2NiO_4 as Catalyst Precursor60 Characterization of Carbon Deposition", *Catalysis Today*, Vol. 133–135, pp. 200-209.

Ji L, S. Tang, H.C. Zeng, J. Lin and K.L. Tan, 2001, "CO_2 Reforming of Methane to Synthesis Gas over Sol-gel-made $Co/\gamma\text{-}Al_2O_3$ Catalysts from Organometallic Precursors", *Applied Catalysis A: General,* Vol. 207, pp. 247-255.

Jiao, H., J. Ren, C. Hua, J. Wang, Z. Cao and Y. Li, 2006, "Density Functional Theory Study into the Adsorption of CO_2, H and CH_x (x = 0-3) as well as C_2H_4 on $\alpha\text{-}Mo_2C(0001)$", *Surface Science*, Vol. 600, pp. 2329-2337.

Kwak, H., K. Kang, H. Kim and I. Shim, 2011, "Catalytic Test of Supported Ni Catalysts with Core/shell Structure for Dry Reforming of Methane", *Fuel Processing Technology,* Vol. 92, pp. 1236-1243.

Liu, J. A., 2006, *Kinetics, Catalysis and Mechanism of Methane Steam Reforming*, M. S. Thesis, Worcester Polytechnic Institute.

Menéndez, J. A., B. Fidalgo, L. Zubizarreta, J.M. Bermúdez and A. Arenillas, 2010, "Synthesis of Carbon-supported Nickel Catalysts for the Dry Reforming of CH_4", *Fuel Processing Technology,* Vol. 91, pp. 765-769.

Mirodatos, C., R. Bouarab, O. Akdim, A. Auroux and O. Cherifi, 2004, "Effect of MgO Additive on Catalytic Properties of Co/SiO_2 in the Dry Reforming of Methane", *Applied Catalysis A: General*, Vol. 264, pp. 161-168.

Mondal K. C., V. R. Choudhary and U. A. Joshi, 2007, "CO_2 Reforming of Methane to Syngas over Highly Active and Stable Supported CoO_x (accompanied with MgO, ZrO_2 or CeO_2) Catalysts", *Applied Catalysis A: General,* Vol. 316, pp. 47-52.

Gallego, G. S., Mondragón, F., C. Batiot-Dupeyrat, J. Barrault and E. Florez, 2008, "Dry Reforming of Methane over $LaNi_{1-y}B_yO_{3\pm\delta}$ (B=Mg, Co) Perovskites Used as Catalyst Precursor", *Applied Catalysis A: General,* Vol. 334, pp. 251-258.

Michaelides, A. and P. Hu, 1999, "Methyl Chemisorption on Ni(111) and C-H-M Multicentre bonding: A Density Functional Theory Study", *Surface Science*, Vol. 437, pp. 362.

Montoya J.A., E. Romero-Pascual, C. Gimon, P. Del Angel and A. Monzón, 2000, "Methane Reforming with CO_2 over Ni/ZrO_2-CeO_2 Catalysts Prepared by Sol-gel", *Catalysis Today*, Vol. 63, pp. 71-85.

Nagaoka K., K. Takanabeb and K. Aika, 2004, "Modification of Co/TiO_2 for Dry reforming of Methane at 2 MPa by Pt, Ru or Ni", *Applied Catalysis A: General*, Vol. 268, pp. 151-155.

Nagaoka K., M. Okamura and K. Aika, 2001, "Titania Supported Ruthenium as a Coking-Resistant Catalyst for High Pressure Dry Reforming of Methane", *Catalysis Communications*, Vol. 1, pp. 255-260.

Osaki T. , H. Masuda and T. Mori, 1994, "Intermediate Hydrocarbon Species for the CO_2-CH_4 Reaction on Supported Ni Catalysts", *Catalysis Letter*, Vol. 29, pp. 33-37.

O'Shea, V., S. González, F. Illas, J. L.G. Fierro, 2008, "Evidence for Spontaneous CO Activation on Cobalt Surfaces", *Chemical Physics Letters*, Vol. 454, pp. 262-268.

Özkara-Aydınoğlu Ş. and A. E. Aksoylu, 2010, "Carbon Dioxide Reforming of Methane over Co-X/ZrO_2 Catalysts (X=La, Ce, Mn, Mg, K)", *Catalysis Communications*, Vol. 11, pp. 1165-1170.

Özkara-Aydınoğlu, Ş., E. Özensoy and A. E. Aksoylu, 2009, "The Effect of Impregnation Strategy on Methane Dry Reforming Activity of Ce Promoted Pt/ZrO_2", *International Journal of Hydrogen Energy,* Vol. 33, pp. 9711-9722.

Papadopoulou, Ch., A. Kambolis, H. Matralis, A. Trovarelli and Ch. 2010, "Ni/CeO_2-ZrO_2 Catalysts for the Dry Reforming of Methane", *Applied Catalysis A: General*, Vol. 377, pp. 16-26.

Payne, M. C., M. P. Teter, D. C. Allan, T. A. Arias and J. D. Joannopoulos, 1992, "Iterative Minimization Techniques for *ab initio* Total-energy Calculations: Molecular Dynamics and Conjugate Gradients", *Reviews of Modern Physics*, Vol. 64, pp. 1045.

Pick, S., 2007, "Density-functional Study of the CO adsorption on Ferromagnetic Co(0001) and Co(111) Surfaces", *Surface Science,* Vol. 601, pp. 5571-5575.

Rodrígunez-Ramos, I., P. Ferreira-Aparicio and A. Guerrero-Ruiz, 1998, "Comparative Study at Low and Medium Reaction Temperatures of Syngas Production by Methane Reforming with Carbon Dioxide over Silica and Alumina Supported Catalysts", *Applied Catalysis A: General*, Vol. 170, pp. 177-187.

Román-Martínez, M.C., D. San-José-Alonso, J. Juan-Juan and M.J. Illán-Gómez, 2009, "Ni, Co and Bimetallic Ni-Co Catalysts for the Dry Reforming of Methane", *Applied Catalysis A: General,* Vol. 371, pp. 54-59.

Rostrupnielsen, J. R. and J. H. B. Hansen, 1993, "CO_2-Reforming of Methane over Transition Metals", *Journal of Catalysis*, Vol. 144, pp. 38-49.

Ruckenstein E. and H. Y. Wang, 2002, "Carbon Deposition and Catalytic Deactivation during CO_2 Reforming of CH_4 over Co/γ-Al_2O_3 Catalysts", *Journal of Catalysis*, Vol. 205, pp. 289-293.

San-José-Alonso D., J. Juan-Juan, M.J. Illán-Gómez and M.C. Román-Martínez, 2009, "Ni, Co and Bimetallic Ni-Co Catalysts for the Dry Reforming of Methane", *Applied Catalysis A: General*, Vol. 371, pp. 54-59.

Scelza, O. A., A. D. Ballarini, S. R. de Miguel, E. L. Jablonski and A. A. Castro, 2005, "Reforming of CH_4 with CO_2 on Pt-supported Catalysts Effect of the Support on the Catalytic Behaviour", *Catalysis Today,* Vol. 107-108, pp. 481-486.

Segall, M. D., C.J. Pickard, R. Shah and M. C. Payne, 1996, "Population Analysis in Plane Wave Electronic Structure Calculations", *Molecular Physics*, Vol. 89, pp. 571-577.

Steen, E., J. C. W. Swart, I. M. Ciobîcă and R. A. van Santen, 2008, "Intermediates in the Formation of Graphitic Carbon on a Flat FCC-Co(111) Surface", *Journal of Physical Chemistry C,* Vol 112, pp. 12899-12904.

Sullivana, N. P., N. E. McGuirea, O. Deutschmannb, H. Zhu and R. J. Keea, 2010, “Dry Reforming of Methane in a Stagnation-flow Reactor Using Rh Supported on Strontium-substituted Hexaaluminate”, *Applied Catalysis A: General,* Vol. 394, pp 257-265.

Sumer, A., M. A. Gulmen and A. E. Aksoylu, 2006, "A Theoretical Investigation on $Pt_3Sn(102)$ Surface Alloy and CO-$Pt_3Sn(102)$ System", *Surface Science*, Vol. 600, pp. 2026-2039.

Takanabe K, K Nagaoka, K. Nariai and K. Aika, 2005, “Titania-supported Cobalt and Nickel Bimetallic Catalysts for Carbon Dioxide Reforming of Methane”, *Journal of Catalysis*, Vol. 232, pp. 268-275.

Therdthianwong S., A. Therdthianwong, C. Siangchin and S. Yongprapat, 2008, “Synthesis Gas Production from Dry Reforming of Methane over Ni/Al_2O_3 Stabilized by ZrO_2”, *International Journal of Hydrogen Energy,* Vol. 33, pp. 991-999.

Wang H.Y. and E. Ruckenstein, 2000, “Carbon Dioxide Reforming of Methane to Synthesis Gas over Supported Rhodium Catalysts: The Effect of Support”, *Applied Catalysis A: General*, Vol. 204, pp. 143-152.

Wang H. Y. and E. Ruckenstein, 2001, “CO_2 Reforming of CH_4 over Co/MgO Solid Solution Catalysts-effect of Calcination Temperature and Co Loading”, *Applied Catalysis A: General*, Vol. 209, pp. 207-215.

Wang S., X. Liao, J. Hu, D. Cao, Y. Li, J. Wang and H. Jiao, 2007, “Kinetic Aspect of CO_2 Reforming of CH_4 on Ni(111): A Density Functional Theory Calculation”, *Surface Science*, Vol. 601, pp. 1271-1284.

Yamada, M., K. Omata, N. Nukui, T. Hottai and Y. Showa, 2004, “Strontium Carbonate Supported Cobalt Catalyst for Dry Reforming of Methane under Pressure”, *Catalysis Communications*, Vol. 5, pp. 755-758.

Yang, Y., D. Liu, W. N. E. Cheo, Y. W. Y. Lim, A. Borgna and R. Lau, 2010, "A Comparative Study on Catalyst Deactivation of Nickel and Cobalt Incorporated MCM-41 Catalysts Modified by Platinum in Methane Reforming with Carbon Dioxide", *Catalysis Today*, Vol. 154, pp. 229-236.

Zu, X., S. Ma, Z. Jiao and X. Zhang, 2008, "A Test of Empirical Correction to Site Preference: DFT Calculations for CO Adsorption on Co(0001) Surface", *Journal of Molecular Structure: THEOCHEM*, Vol. 864, pp. 68-71.

Zhu, Q., L. Chen, Z. Hao, T. Zhang and Z. Xie, 2010, "Development of a Co-Ni Bimetallic Aerogel Catalyst for Hydrogen Production via Methane Oxidative CO_2 Reforming in a Magnetic Assisted Fluidized Bed", *International Journal of Hydrogen Energy,* Vol. 35, pp. 8494-8500.

Zhu Y., D. Chen, X. Zhou and W. Yuan, 2009, "DFT Studies of Dry Reforming of Methane on Ni Catalyst", *Catalysis Today*, Vol. 148, pp. 260-267.